Flow Measurement by Acoustic Scintillation in Hydroelectric Intakes

September 2011

1.0 ASFM Operation for Low-Head Hydroelectric Plants

The Acoustic Scintillation Flow Meter (ASFM) measures the discharge (volume flow) of water through a hydroelectric turbine. The acoustic scintillation drift is used to measure the flow speed of water perpendicular to a number of acoustic paths established across the intake to the turbine. The components of the turbulent velocity and refractive-index field along the axis of the acoustic paths give rise to fluctuations in the received acoustic signals. Over sufficiently short time scales the turbulent velocity fluctuations are transported without change with the flow. The ASFM measures the acoustic fluctuations (called scintillations) of a number of closely spaced beams and from their inter-comparison, computes the lateral average of the flow speed and direction perpendicular to each acoustic path. The ASFM measures the discharge through the passage by integrating the perpendicular component of the flow speed from a number of paths spaced over the height of the intake.

Since the scintillation technique was first introduced for the precision measurement of flow rates in hydroelectric plants, accumulated experience has identified certain features of the turbulent flow generated by the trashrack which appear to be common to most plants. This report describes their influence on the performance of the original scintillation system and the algorithms developed account for their effects. The discussion is confined to issues which are fundamental to the application of the technique to hydroelectric plants, and does not consider site specific issues such as non-uniform intake flow distributions. The examples presented here are chosen to illustrate specific points relevant to the development of the algorithms.

The ASFM consists of five major components (see Figure 1):

1) Transducers and cabling (underwater)
2) Switching canisters (underwater)
3) Surface connection cables
4) Surface Control Unit
5) PC computer for control and user interface

The transducers are normally installed on the sides of a fixed or travelling support frame that fits into an intake gate or stoplog slot (installation directly on the walls of the intake is possible if no slots are available). In the three-bay multi-level version of the ASFM, they are divided into three groups. Each group consists of a set of transducers, in pairs, two switching canisters, the cabling connecting the transducers to the switching canisters and the surface connection cables running from the switching canisters to the data acquisition and control module. There may be up to 10 transducer pairs in each group. All pairs in one group would normally be deployed as measurement levels in one intake bay, with the other two groups deployed in the remaining two bays of a three bay intake. All three groups are controlled from the single data acquisition and control module. The ASFM may be deployed in different configurations, for example, two groups of 10 could be installed in a single bay to sample at 20 elevations.

The Surface Control Unit is a self-contained unit that controls the operation of the ASFM, generates and transmits the acoustic signals, and sends the received signals to the computer which calculates the flow velocity for each path. When deployed, it must be placed within 80 meters of the switching canisters (set by the length of the surface connecting cables) and requires shelter from the weather and working space for an operator. The PC is the host computer for the ASFM Link software. ASFM Link provides a graphical user interface (GUI) used to control one or more Surface Control Units. Velocities data calculated from the acoustic data received from the Surface Control Units are used to compute the total flow (discharge) through the turbine.

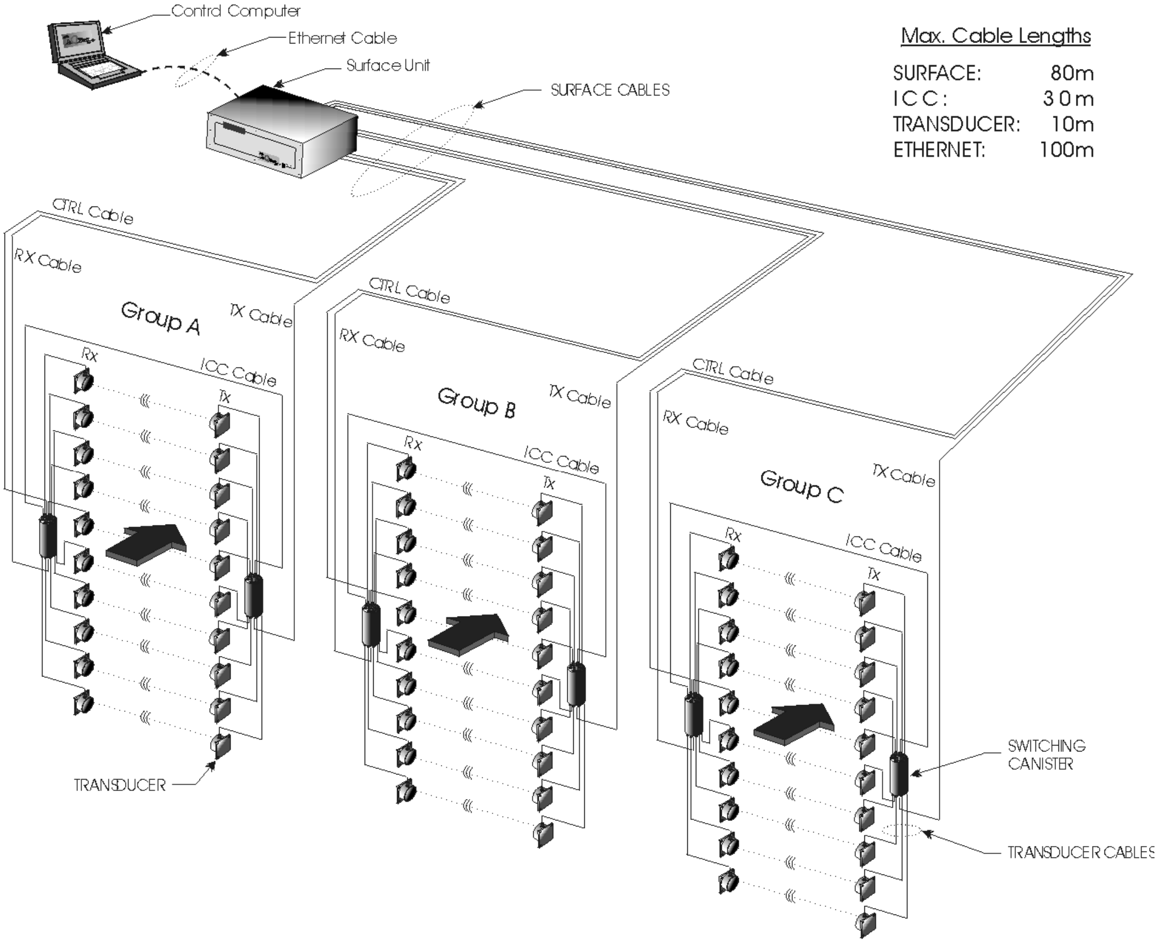

Figure 1.1. Major ASFM system components shown, with the maximum number of transducers.

The ASFM measures the flow speed simultaneously on one path in each bay. Normally, the transducers are placed such that the paths are at the same elevation in each bay. After sampling at the first level is complete, the ASFM computes the flow speed for each path and then switches to the next level. The process is repeated until all levels have been sampled. (The ASFM can also be set up to allow for a support frame with a reduced number of paths to be moved through a series of elevations.) The usual sampling sequence is from the intake floor to the roof. Once sampling is completed on the last level, ASFM Link computes the discharge for each bay and sums the individual results to obtain the total discharge. The individual discharges and the flow speeds are then written to a file, and the ASFM is ready for a new measurement cycle.

2.0 Velocity Calculation, Original Method

Figure 2.1 shows the configuration of the arrays used by the ASFM. Each of these arrays consists of three elements, normally oriented as shown, with the x-axis directed into the intake, the y-axis directed vertically and the z-axis (not shown) directed across the intake. The pair of arrays forming each ASFM level face each other along the z-axis. The quantities d_i and φ_i are fixed properties of each array, while U and θ are the speed and direction of the flow at the level of each array pair.

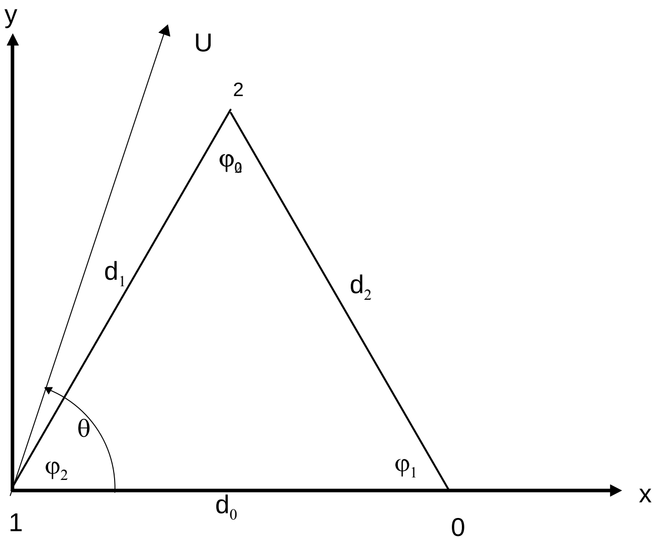

Figure 2.1. Array element orientation and definition of flow vector.

Figure 2.2 defines the flow of data through the ASFM, from the acoustic signal at the transducer to the output velocity. The acoustic transmissions for one level are time-division multiplexed among the three elements of the array (channels 0, 1, and 2). The nominal ping rate of 250 Hz, is adjusted at each level to prevent interference among the elements caused by multiple reflections of the transmissions from the sides of the intake. A section of the software calculates the arrival times for up to 12 reflections, and adjusts the ping rate to eliminate simultaneous arrivals with later transmissions. The arriving analogue signals are digitized, and the peak value of the pulse envelope is computed by quadratic interpolation. The peak values from successive pulses are stored to form discrete time series of the acoustic amplitude at each element for a period which can be varied between 30 seconds and 5 minutes. The series are split into overlapping blocks, and the normalized cross-covariance for each block is computed for each element pair in an array (0-1, 0-2, 1-2). The peak value and the delay to the peak are computed for each normalized cross-covariance curve. These quantities are then combined to compute the magnitude, U, and inclination, θ of the flow velocity, as described below.

Under conditions of uniform distribution of turbulent kinetic energy, where the spectrum of the turbulence may be assumed to be homogeneous and isotropic, and therefore to follow the Kolmogorov spectral form, the log-amplitude cross-covariance for spherical waves propagating from coherent transmitters over parallel paths to two receivers is given by (Lee & Harp, 1969):

$$C_\chi = 4\pi^2\alpha^2 k^2 C_n^2 \int_0^L \int_0^\infty K^{-8/3} \sin^2\left[\frac{K^2 z(L-z)}{2kL}\right] J_0\left(K\left|\vec{\rho}-\vec{V}\tau\right|\right) dK dz \tag{2.1}$$

Since the Bessel function J_0 has no dependence on z, the peak of C_χ for each value of the turbulence wavenumber K occurs when $\left|\vec{\rho}-\vec{V}\tau\right|$ is a minimum. For the log-amplitude covariance, only wavenumbers K, which are near $\sqrt{\lambda L}$ contribute significantly, so that only the main lobe of the Bessel function need be considered.

Define three acoustic paths and the flow vector as shown in Figure 2.1. The x-axis is oriented horizontally, positive toward the turbine. The y-axis is oriented vertically, positive upwards. Angles increase counter-clockwise from zero along the x-axis. The inter-element separations d_0, d_1, and d_2 are known quantities, and the associated angles φ_0, φ_1, and φ_2 may be calculated from the Law of Cosines and the Law of Sines:

$$\cos\varphi_2 = \frac{d_0^2 + d_1^2 - d_2^2}{2d_0 d_1}$$

$$\frac{d_0}{\sin\varphi_0} = \frac{d_1}{\sin\varphi_1} = \frac{d_2}{\sin\varphi_2}$$

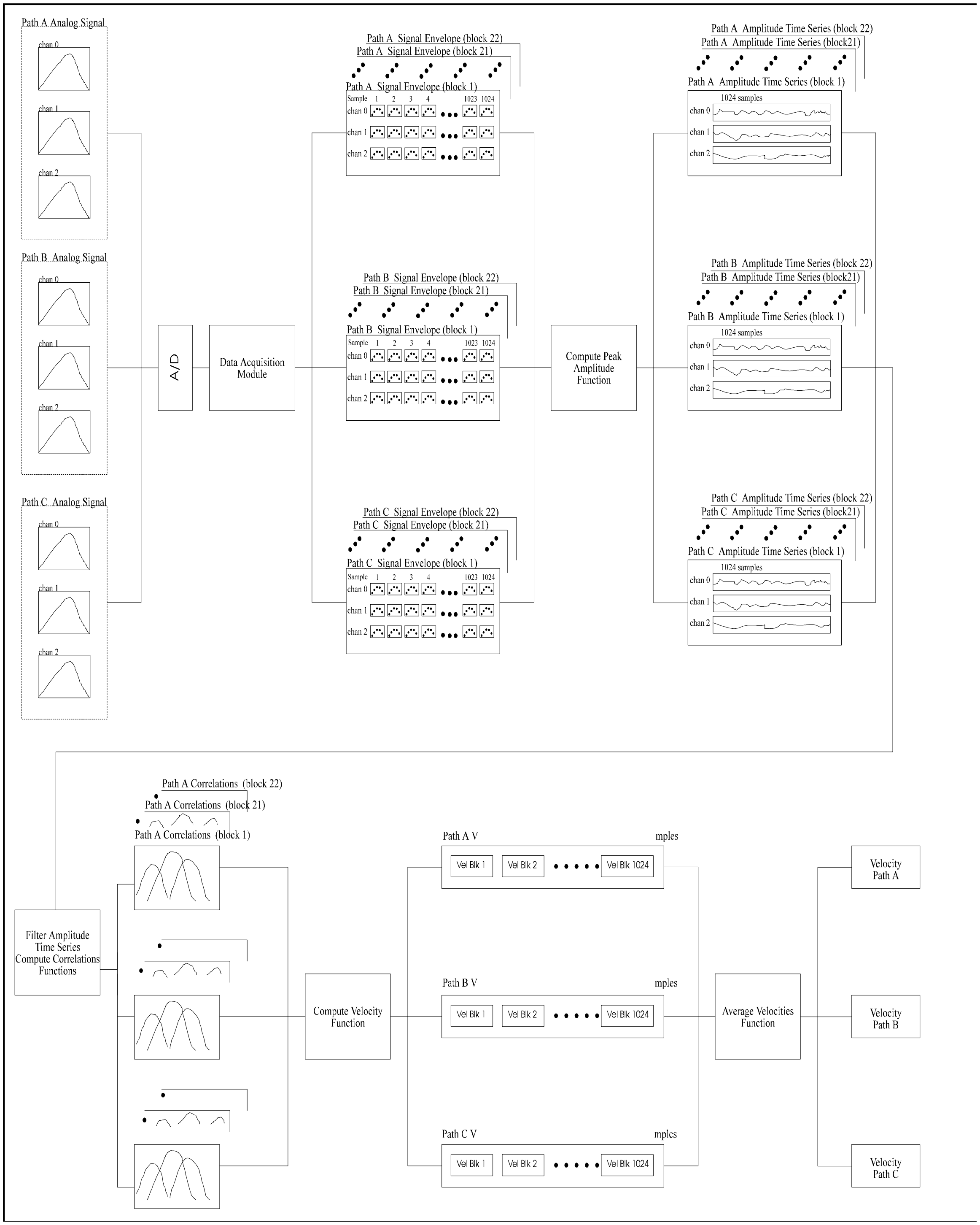

Figure 2.2. Flow of data and calculations through the ASFM

The path separation vectors and the flow vector are then defined as:

$$\overline{d}_0 = (d_0, 0)$$

$$\overline{d}_1 = (d_1 \cos\varphi_2, d_1 \sin\varphi_2)$$

$$\overline{d}_2 = (d_2 \cos\varphi_1, -d_2 \sin\varphi_1)$$

$$\overline{U} = (U\cos\theta, U\sin\theta)$$

The lag to the peak of the cross-covariance, C_χ, for each transducer pair will be found at the point at which

$$\partial\left(\left|\overline{d} - \overline{U}\tau\right|^2\right) / \partial\tau = 0$$

In the case of the pair defined by d_0,

$$\left|\overline{d} - \overline{U}\tau\right|^2 = (d_0 - U\tau\cos\theta)^2 + U^2\tau^2\sin^2\theta$$

$$\frac{\partial}{\partial\tau}\left(\left[(d_0 - U\tau\cos\theta)^2 + U^2\tau^2\sin^2\theta\right]\right) = 2U^2\tau - 2d_0U\cos\theta$$

The derivative will be a minimum at

$$\tau_0 = \frac{d_0\cos\theta}{U} \tag{2.2}$$

Similarly, the delay to the peak of the cross-covariance for the other two path pairs is given by:

$$\tau_1 = \frac{d_1\cos(\theta - \varphi_2)}{U} \tag{2.3}$$

$$\tau_2 = \frac{d_2\cos(\theta + \varphi_1)}{U} \tag{2.4}$$

The best estimate of the velocity $\overline{U} = (U\cos\theta, U\sin\theta)$ is found by finding the values of U and θ which, when substituted in the expressions above for τ_0, τ_1, and τ_2 give the best match to the measured values of the peak lags. Since there are three relations to be satisfied with only 2 free parameters, that is an over-determined system of equations, and there will not be an exact solution.

The best approximation can be defined in the least-squares sense as the values of *U* and *θ* which minimize

$$\mathrm{E}(U,\theta)=\sum_i (\tau_i - F(U,\theta)_i)^2$$

where *i* = (0,1,2), and

$$F(U,\theta)=\begin{bmatrix} \dfrac{d_0 \cos\theta}{U} \\ \dfrac{d_1 \cos(\theta-\varphi_2)}{U} \\ \dfrac{d_2 \cos(\theta+\varphi_2)}{U} \end{bmatrix}$$

The values for *U* and *θ* which minimize E(U,*θ*) may be calculated using a standard non-linear minimization algorithm, such as the Levenberg-Marquardt method, which was selected for the ASFM data.

As currently configured the triangular array is equilateral. The nomenclature followed in the remainder of the report refers to the correlation pairs as follows:

1-0 as the Horizontal pair

1-2 as the Vertical pair

2-0 as the Diagonal pair

This convention originates from an earlier design of array having the form of a right-angled triangle, in which the side 1-2 was vertical, and side 1-0 aligned with the intake horizontal reference. The nomenclature is retained here as it is adopted for much of the extant ASFM literature.

The following sections analyze the effects on the accuracy of the velocity measurement by acoustic scintillation when the turbulence in the intake does not conform to the assumptions of homogeneity and isotropy used in the original form of the algorithm.

3.0 Revisions to the algorithm to account for anisotropy of the turbulent field

The original algorithm outlined in section 2.0 is based on the assumptions that the turbulence is isotropic, and is homogeneous along the length of the acoustic path, and that the characteristics are unchanged during the transit time across the triangular transducer array. When installed in a typical short length hydroelectric intake, the assumptions of isotropy and homogeneity along the path length may often be violated, with consequent errors in the output of the scintillation system.

The combination of non-uniformities in the intensity of the turbulence and the magnitude of the mean velocity along the path length gives rise to a bias in the path averaged speeds and flow angles. These conditions arise from non-uniform intake conditions generated by substantial structural members such as pillars upstream of the measurement plane or cross flows at the entrance. This is a site specific issue and requires additional vertical acoustic paths and/or CFD modeling for its resolution and will be considered in general terms in Section 14.

Some degree of anisotropy is present in the turbulence generated by the trashracks of most hydroelectric intakes, and is manifest in the correlation data of the scintillation system. The detection and correction for the effects of this anisotropy are the primary focus of the present report. The turbulence generated by the typical trashrack consists of two distinct components, a small scale relatively uniform turbulence generated by the array of vertical fine bars, superimposed on a set of interacting wakes generated by the larger structural members of the supporting grid. In addition, the resulting turbulent field may be further distorted by an overall shear in the mean velocity distribution. The resulting turbulence field is often far from uniform, and rapidly changing as the flow progresses through the intake. The position of the ASFM measurement plane relative to the trashrack thus determines the nature of the turbulence sampled.

Data from the following plants are presented to illustrate particular aspects of the data analysis and the associated algorithms.

Kennebec Units 1 and 2.
This plant has a steep roof angle the resulting wide range of flow angles provided the first clear evidence of the effects of anisotropy. In Unit 2 this was combined with a non-uniform intake flow.

Lower Granite, with and without fish deflection screens.
This is a case where the same basic intake geometry had very different internal flow distributions, and in addition, simultaneous the tests were performed with an independent measurement system, Wittinger (2007).

Kootenay Canal
Here the scintillation system was operated as part of a comprehensive performance evaluation including two other measurement systems against a standard reference. Almquist, (2011).

Little Goose.

Tests at a single level with extended time series explore issues of the statistical stability of the correlations.

Two other low-head Kaplan plants, CNR and Wells are also used in specific illustrations.

3.1 The internal consistency of ASFM data

The isotropy condition implies that the cross-correlation coefficient between a pair of sensor outputs depends only on their separation distance, and is independent of their orientation with respect to the flow. The peak values of the cross-correlation curves are then determined by the characteristics of the turbulence and the effective separation of the sensors, the latter being directly related to the flow angle. If the form of correlation field is known, the peak correlation values themselves provide information as to the flow angle. The correlation peak magnitudes and their time delays thus in principle provide two independent means of determining the flow angle.

Two specific flow directions provide a check on the self-consistency of the data when subject to the assumption of local isotropy. For these conditions a comparison of the ratios of the time delays and of the peak correlation values provides a check on the internal consistency of the flow properties returned by the original ASFM algorithm.

Case 1. Normal incidence.

If the flow is normal to the line of a pair of transducers, for example $\theta = 330^o$, the time delay between the vertical pair is zero, and those between the horizontal and diagonal pairs are equal. The corresponding correlation peaks are a minimum for the vertical pair, and equal for the remaining pair.

Case 2. Parallel incidence

If the flow is parallel to the line of a pair of transducers, a similar situation arises, with the difference that the time delay and correlation peak are a maximum for that pair, and those of the remaining pairs equal.

The following examples illustrate the inconsistencies found in the data from the Kennebec plant where the flow angles returned by the ASFM algorithm differed appreciably from those predicted by a CFD numerical simulation of the intake. The steep roof angle of this plant provides flow angles approximately normal to the vertical transducer pair in a number of cases. Table 3.1 lists the individual tests where the approach angle returned by the original ASFM algorithm is either approximately 330^o, or the appropriate time delays are equal. It can be seen that for all the cases listed, the symmetry of the correlation peaks is violated, there being significant differences between the two values. Comparing Units 1 and 2, the discrepancies are mainly confined to the upper levels of Unit 1, but for unit 2 are distributed much lower down the intake. The region covered by the correlation peak mismatch coincides almost exactly with the mismatch between the flow angles derived from the ASFM and a detailed CFD study of these inlets.

Near the center of the intake, the flow angle is almost parallel to the horizontal pair, and Case 2 occurs. Table 3.2 lists the individual test results where this condition is satisfied, either by the flow angle, or the time delays. In this case the data are self-consistent, and the computed angles for both units closely match the CFD results. Note should also be taken of the relatively high correlation coefficients for the horizontal pair of 0.97, an indication that the turbulence does not evolve significantly during the transit time. Figures 3.1 (a) and (b) below show the symmetric pairs of correlation peaks graphically, and the discrepancy for the normal incidence case can be clearly seen. It will be shown that these inconsistencies result from anisotropy in the turbulent field which systematically displaces the correlation peaks, modifying the time delays.

Table 3.1 Kennebec plant, case 1

Unit	Level	Test no.	Angle deg	Horiz peak	Horiz delaysec.	Vertical Peak	Vertical delay sec.	Diagonal peak	Diagonal delay sec.
1	16	1	333.2	0.901	0.014	0.49	-0.001	0.674	0.014
1	16	4	329.6	0.885	0.014	0.489	-0.002	0.712	0.015
1	16	5	329.1	0.901	0.013	0.411	-0.002	0.607	0.015
1	15	0	332.1	0.884	0.015	0.432	0	0.606	0.015
1	15	1	336.6	0.885	0.016	0.437	0.001	0.622	0.014
1	15	2	331.8	0.917	0.016	0.521	0	0.645	0.015
1	15	4	335.4	0.877	0.016	0.427	0	0.613	0.014
1	12	6	331.4	0.931	0.017	0.478	0.000	0.613	0.016
2	16	0	334.8	0.878	0.013	0.413	0	0.651	0.012
2	16	1	326.0	0.904	0.012	0.467	-0.001	0.659	0.013
2	16	6	331.3	0.897	0.012	0.421	-0.001	0.653	0.013
2	16	7	327.8	0.901	0.013	0.431	-0.001	0.671	0.014
2	15	1	329.0	0.925	0.013	0.474	-0.001	0.687	0.013
2	15	2	332.6	0.935	0.013	0.449	0	0.639	0.012
2	15	3	337.7	0.893	0.013	0.445	0.001	0.669	0.012
2	15	4	328.5	0.88	0.013	0.313	-0.001	0.58	0.013
2	15	5	334.4	0.884	0.013	0.379	0	0.652	0.013
2	14	1	334.8	0.923	0.015	0.472	0	0.689	0.014
2	14	2	333.7	0.927	0.015	0.364	0.001	0.59	0.013
2	13	1	336.0	0.913	0.016	0.53	0.001	0.729	0.014
2	13	2	331.7	0.893	0.015	0.522	0	0.688	0.015
2	13	6	337.5	0.933	0.015	0.441	0.001	0.609	0.013
2	12	1	335.5	0.938	0.016	0.432	0.001	0.641	0.016
2	12	4	331.9	0.945	0.016	0.617	-0.001	0.743	0.016
2	11	5	334.10	0.951	0.018	0.47	0	0.614	0.018
2	10	6	333.4	0.928	0.019	0.58	0.001	0.703	0.017

Table 3.2. Kennebec plant, case 2.

Unit	Level	Test no.	Angle deg	Horizontal peak	Horizontal delay sec.	Vertical peak	Vertical delay sec.	Diagonal peak	Diagonal delay sec.
1	10	2	359.6	0.953	0.019	0.551	0.01	0.623	0.01
1	8	2	360.0	0.971	0.017	0.614	0.009	0.617	0.009
1	8	3	1.2	0.955	0.018	0.55	0.01	0.593	0.009
1	8	4	359.4	0.967	0.018	0.607	0.009	0.646	0.009
1	7	3	0.07	0.967	0.017	0.591	0.009	0.634	0.008
1	6	3	0.9	0.967	0.018	0.642	0.01	0.675	0.009
2	7	0	359.81	0.94	0.022	0.541	0.012	0.612	0.011
2	6	4	359.2	0.96	0.023	0.501	0.011	0.577	0.012
2	4	1	359.6	0.963	0.021	0.562	0.01	0.534	0.011

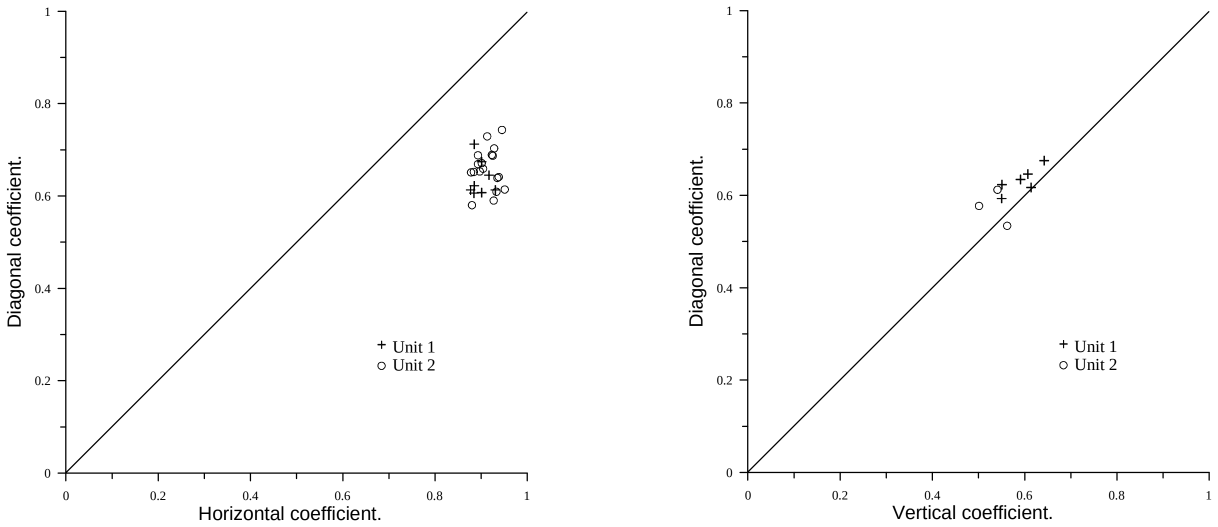

Figure 3.1. Kennebec data, (a) normal incidence. (b) parallel incidence.

4.0 The consequences of an anisotropic correlation field

Consider the situation illustrated in figure 4.1, where the contours of the correlation field are elliptical rather than the circular form of isotropic turbulence assumed for the algorithm.
The three time series of the transducer array represent slices across the correlation field, the position of the correlation peak corresponding to the tangent point to the local contour; the offset Δx represents an additional component of the time delay which gives rise to the

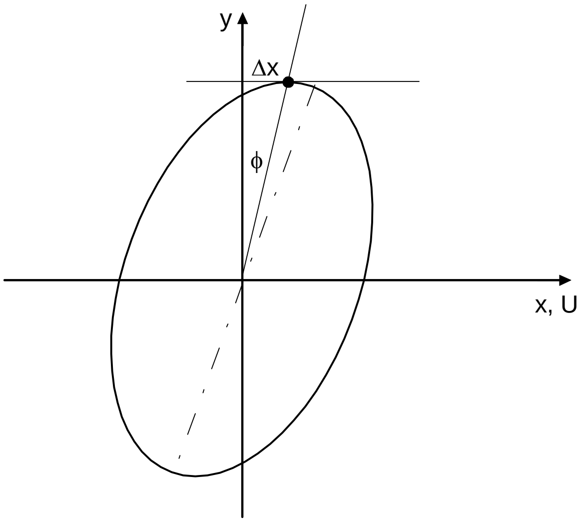

Figure 4.1. Sketch of a 2-D anisotropic correlation field.

discrepancy in the flow angle and a corresponding error in the flow speed. If the correlation contours are self similar, ie they differ only by a scale factor, the locus of the correlation peaks is a radial line. If the form of the correlation function is known along this line, the flow angle can be deduced from the peak cross corrrelation values. Note that if either the major or minor axis of the ellipse is aligned with the y-axis, the time delays are undistorted, and the original algorithm based on the time delays provides the correct flow speed and direction.

The time delays represent the projections of the sides of the array onto the flow direction, and the following condition is a property of the triangular geometry of the array. Under ideal conditions,

$$\Delta T_V + \Delta T_D - \Delta T_H = 0 \,,$$

or normalizing by d/U, the transit time across the array, we define:

$$\text{Scaled checksum, } S = \frac{U(\Delta T_V + \Delta T_D - \Delta T_H)}{d} \qquad (4.1)$$

For the condition $S = 0$ to be satisfied, it is sufficient for the locus of the correlation peaks to lie on a radial line. In practice, S invariably differs from zero, and it will be subsequently shown that for a typical hydro-electric plant intake, this is associated with the degree of anisotropy of the turbulence and the orientation of the transducer array. The non-zero checksum values introduce a small systematic error in the flow angle calculation. The upper bounds on these errors are discussed in section 12.

4.1 The correlation field

To make use of the information contained in the correlation peak values, it is necessary to make assumptions as to the form of the 2-D path average correlation field. The only detailed information provided by the ASFM as to the form of the correlation field is from the auto-correlation function. Figure 4.2 compares examples of auto-correlation functions from hydro-electric plant intakes covering a wide range of geometries. The correlation distances of the individual curves have been scaled by the first zero crossing point, with the exception of the Kennebec Unit 2 data, where the shape differs considerably from the other examples at the lower levels. In this case the distance has been scaled to match the auto-correlation function to the other plants at a correlation of 0.4, the lower limit of the cross correlations for this data set.

With the exception of the Kennebec data, the auto-correlation functions from a variety of intakes are surprisingly similar up to the zero crossing point. Shown for comparison is the theoretical covariance function of Lee and Harp (1969) for the parallel path case with the Kolmogorov turbulent spectrum employed in most theoretical analyses of scintillation systems. As can be seen, this differs appreciably from the functions observed in the hydro-electric plant intakes.

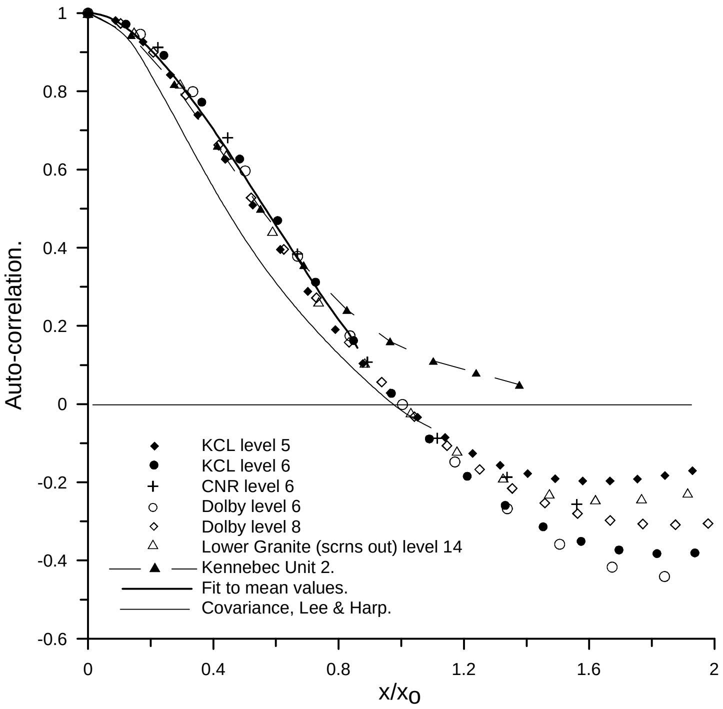

Figure 4.2. Measured auto-correlation functions, scaled distances.

The lowest value of cross-correlation peak which can be unambiguously interpreted in practice is about 0.2, and within this useable range, the measured auto-correlation functions of figure 4.2 can be closely approximated by the Gaussian function.

$$f_n = \exp(-\alpha x^2) \qquad (4.2)$$

Figure 4.3 compares the mean of the experimental auto-correlation functions of figure 4.2 with the Gaussian function of (4.2), where the length scales have now been chosen to match the curves at a correlation value of 0.3.

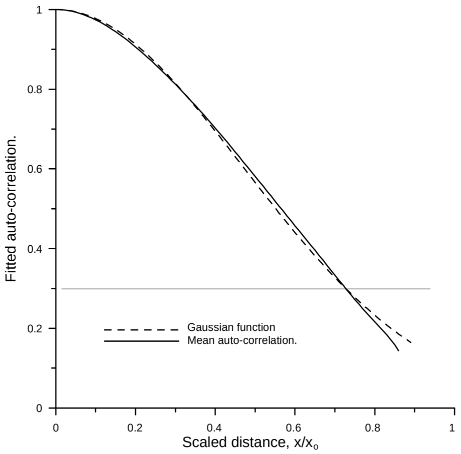

Figure 4.3. Comparison between the Gaussian and the mean auto-correlation function.

5.0 An exact solution for the flow angle derived from the correlation peaks

The strong similarity between the shapes of the auto-correlation functions from a wide range of intakes and their similarity to the Gaussian function suggests that the latter is a suitable candidate for adoption as characteristic shape for the general correlation field.

The Gaussian function of equation (4.2) is slightly modified to allow for a small additional de-correlation, having the general form:

$$f_r = a\exp(-\alpha r^2) \qquad (5.1)$$

The parameters a and α are fitting constants, the parameter a, which should be close to unity, provides a measure of the overall quality of the correlation. The parameter α is a measure of the correlation scale length $\sigma\,(=\alpha^{-1/2})$,a function of the general direction ϕ of the correlation. If it is assumed that the correlation peaks lie on a radial line in the direction ϕ_P, the three values are then sufficient to provide an exact solution for the three unknowns, a, α_P and the flow angle θ.

Denoting the correlation peaks as follows:

Horizontal $$f_H = a\exp\left[\frac{-\alpha_P d^2 \sin^2(\theta)}{\cos^2\phi_P}\right] \qquad (5.2)$$

Vertical $$f_V = a\exp\left[\frac{-\alpha_P d^2 \sin^2(60-\theta)}{\cos^2\phi_P}\right] \qquad (5.3)$$

Diagonal $$f_D = a\exp\left[\frac{-\alpha_P d^2 \sin^2(60+\theta)}{\cos^2\phi_P}\right] \qquad (5.4)$$

ϕ_P is the off-set angle of the correlation peaks, measured clockwise from the normal to the flow direction, at present unknown, and d the transducer separation. The above equations can be solved to give the following solution,

$$\tan 2\theta = \frac{\sqrt{3}}{1-2A}, \qquad \text{where } A = \frac{\ln\left(f_H / f_V\right)}{\ln\left(f_D / f_V\right)} \qquad (5.5)$$

$$\frac{\cos^2\phi_P}{\alpha} = \frac{d^2\sqrt{3}\sin(2\theta)}{2\ln(f_d / f_v)}, \qquad (5.6)$$

and

$$\ln a = \alpha_P d^2 \sin^2\theta + \ln f_H \qquad (5.7)$$

The factor $cos^2(\phi_P)/ \alpha_P$ is the square of the correlation scale normal to the flow direction.

The flow angle θ and the factor a are independent of the correlation peak offset angle ϕ_P , which is later identified as the difference between the angle derived from the time delays and the flow angle θ. The above equations return flow angles in the first and fourth quadrants, and angles outside this range must be corrected to the appropriate quadrant by means of the time delays. The details of the solution and the quadrant selection procedure are given in appendix A.

Figures 5.1 and 5.2 compare the flow angle calculated from the correlation peaks with the angle calculated from the time delays and with the CFD calculations for the Kennebec plant Units 1and 2. In the upper parts of the intake the flow angles calculated from the time delays differ by up to 20^o from those calculated from the correlation peaks, and for Unit1, the flow angles calculated from the correlation peaks closely follow the CFD calculations. For Unit 2, the differences between the two flow angle calculations extends about twice as far down the measurement plane, and the flow angles calculated from the correlation peaks differ slightly from the CFD calculations. The CFD calculations for Unit 2 showed a region of separated flow along one wall associated with non-uniform flow distributions at the intake entry. The CFD profiles shown are positioned along the centerline of the intake, while the profiles from the ASFM are the path averages across the intake. The non-uniform flow conditions across the intake accounts for the small difference between the single CFD profile and the path average of the ASFM.

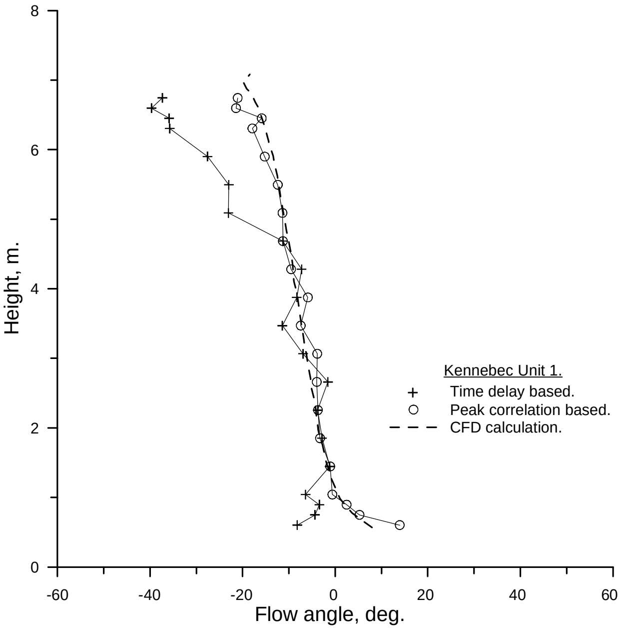

Figure 5.1. Comparison of flow angle algorithms, Kennebec Unit 1.

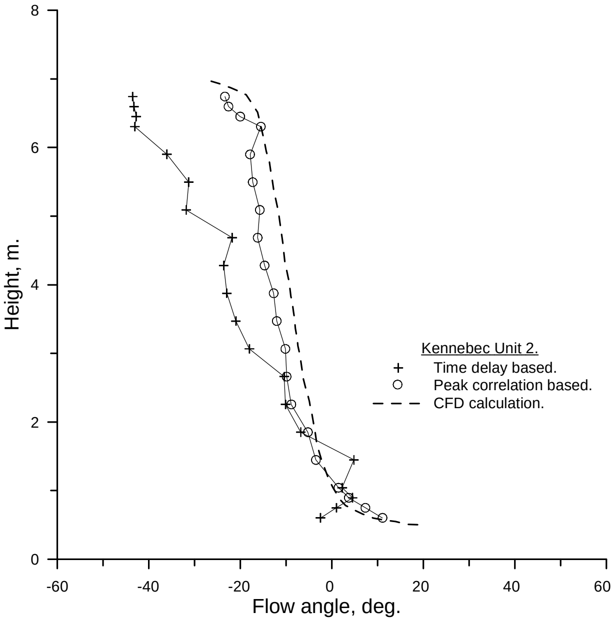

Figure 5.2. Comparison of flow angle algorithms, Kennebec Unit 2.

6.0 The interpretation of the time delays to include a simple anisotropy

The effect of the anisotropy on the time delays can be expressed directly in terms of the correlation peak offset angles. The following diagrams define the geometry of the array and the sign convention adopted for measuring the displacement of the correlation curves, where the peaks are shown displaced by an amount Δx from their expected positions under isotropic conditions. The displacement is shown in the direction most commonly observed in the ASFM data, ie. the difference between the angle returned by the ASFM algorithm and the true flow angle is counter clockwise, negative in the sign convention adopted here. The peak offset angle ϕ_P is thus negative as shown in the diagrams, and the true flow angle θ as positive.

Horizontal pair.

The smaller angle returned by the ASFM algorithm results from the time delay being too long.

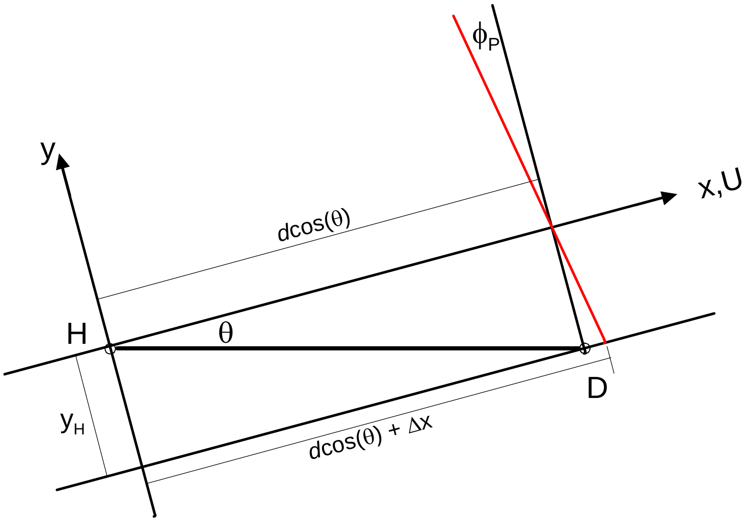

Figure 6.1. The horizontal transducer pair.

The origin is taken at the upstream transducer H, with x positive in the direction of flow and y positive towards the roof. With H as the reference transducer for the cross correlation, the correlation peak is shifted to the right, increasing the time delay. The offset angle ϕ is defined as positive clockwise, and here has been taken to have a negative value.

$$\Delta T_H = \frac{[d\cos(\theta) + \Delta x]}{U}$$

where $\Delta x = y_H \tan(\phi_P)$ and $y_H = -d\sin(\theta)$,

hence
$$\Delta T_H = \frac{d[\cos(\theta) - \sin(\theta)\tan(\phi_P)]}{U} \qquad (6.1)$$

Vertical pair.

In this case underestimating the flow angle corresponds to a shortened time delay.

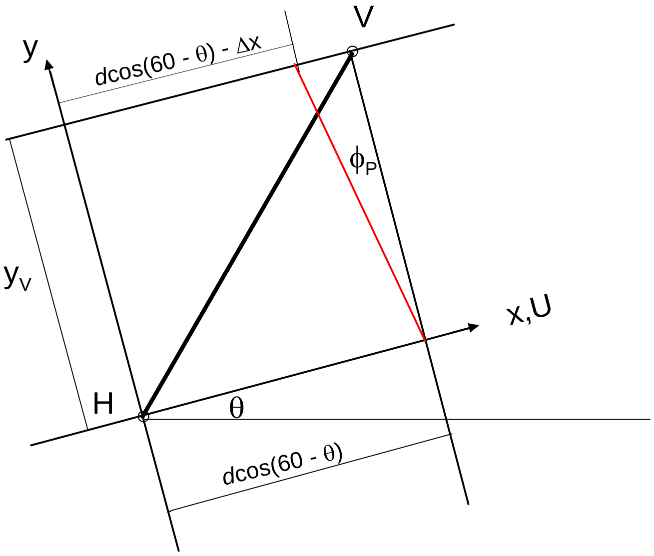

Figure 6.2. Vertical transducer pair.

The reference time series for the cross correlation is again the upstream transducer H, and with

$$y_V = d \sin(60 - \theta)$$

the time delay becomes

$$\Delta T_V = \frac{d\left[\cos(60-\theta) + \sin(60-\theta)\tan(\phi_P)\right]}{U} \qquad (6.2)$$

Diagonal Pair.

As for the case of the horizontal pair, the time delay is extended,

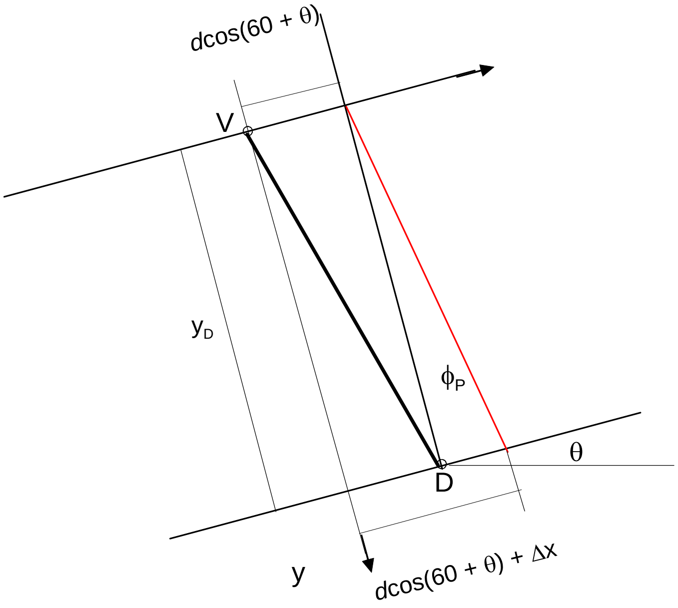

Figure 6.3. Diagonal transducer pair

In this case the vertical transducer is taken as the reference time series to provide a positive time delay relative to the flow direction, consistent with the horizontal and vertical pairs.

$$y_D = -d\sin(60+\theta)$$

hence,

$$\Delta T_D = \frac{d[\cos(60+\theta) - \sin(60+\theta)\tan(\phi_P)]}{U} \qquad (6.3)$$

Note that for flow angles in the upper half plane, the horizontal and diagonal cross correlations are located in the lower half of the correlation plane.

If the peak offset angle ϕ is the same for all three correlation curves, the following relation can be derived between the angles determined from the correlation peaks and from the time delays.

The time delays defined by equations (6.1) and (6.3) have the form of the expanded cosine expression cos(A+B), with equation (6.2) of the form cos(A-B). In the case of the horizontal pair (6.1),

$$\cos(A+B) = \cos A \cos B - \sin A \sin B$$

$$= \cos B(\cos A - \sin A \tan B)$$

Comparing this expression with (6.1), we find the following identities,

$$A \rightarrow \theta, \qquad B \rightarrow \phi_P$$

The expressions for the time delay thus transform to

$$\Delta T_H = \frac{d\cos(\theta + \phi_P)}{U\cos(\phi_P)} \qquad (6.4)$$

Repeating the process for 6.2 and 6.3 yields

$$\Delta T_V = \frac{d\cos[60 - (\theta + \phi_P)]}{U\cos(\phi_P)} \qquad (6.5)$$

$$\Delta T_D = \frac{d\cos[60 + (\theta + \phi_P)]}{U\cos(\phi_P)} \qquad (6.6)$$

In the original algorithm of section 2, it is assumed that the correlation peaks lie along the normal to the flow direction, ie that ϕ_P is zero, and the relationships relating the time delays to the flow speed and direction reduce to,

$$\Delta T_H = \frac{d\cos(\theta')}{U'} \qquad (6.7)$$

$$\Delta T_V = \frac{d\cos(60 - \theta')}{U'} \qquad (6.8)$$

$$\Delta T_D = \left(\frac{d\cos(60 + \theta')}{U'}\right) \qquad (6.9)$$

where U' and θ' are the speed and direction derived from the time delays, and in general differ from those derived from the extended equations 6.4, 6.5 and 6.6.

Equating the corresponding expressions for the time delays yields the relationships

$$\phi_P = \theta' - \theta \tag{6.10}$$

and

$$U' = U \cos\phi_P \tag{6.11}$$

The difference between the flow angles derived from the time delays and the correlation peaks is thus identified with the corelation peak offset angle. The anisotropy introduces a rotation of the velocity vector by the angle ϕ_P and the flow speed and angle returned by the original ASFM algorithm are projections of the true values. The difference between the flow angle derived from the time delays and from the correlation peaks provides for the necessary correction to the flow speed.

7.0 An analytic solution for the angle and speed from time delays

The correction for the anisotropy as developed above retains the solution based on the time delays, and it was found that the convergence criteria of the original Levenberg-Marquardt numerical routine were not always sufficiently rigorous. The least squares problem is amenable to analytical solution, the details of which are presented here.

The problem is posed as the minimization of the least squares residual with respect to the projected flow speed *U'* and the angle *θ'*.

$$\Sigma = \left[\Delta T_H - \frac{d}{U'}\cos\theta'\right]^2 + \left[\Delta T_V - \frac{d}{U'}\cos(60-\theta')\right]^2 + \left[\Delta T_D - \frac{d}{U'}\cos(60+\theta')\right]^2 \tag{7.1}$$

Where *U'* and ***θ'*** are denoted as the isotropic speed and direction, to distinguish them from the true speed and direction *U* and *θ*.

The terms in the residual sum Σ can be expanded to yield

$$\Sigma = (\Delta T_H^2 + \Delta T_V^2 + \Delta T_D^2) + \frac{3}{2}\left(\frac{d}{U'}\right)^2 - \left(\frac{d}{U'}\right)\left(A_0\cos\theta' + \sqrt{3}B_0\sin\theta'\right) \tag{7.2}$$

where $A_0 = (2\Delta T_H + \Delta T_V + \Delta T_D)$ and $B_0 = (\Delta T_V - \Delta T_D)$.

To determine the stationary points of Σ the following conditions must be satisfied

$$\frac{\partial\Sigma}{\partial\theta'} = 0, \qquad \frac{\partial\Sigma}{\partial U'} = 0\text{, and} \qquad \frac{\partial^2\Sigma}{\partial\theta'^2}\frac{\partial^2\Sigma}{\partial U'^2} > \left(\frac{\partial\Sigma}{\partial\theta'\partial U'}\right)^2 \tag{7.3}$$

and for a stationary point to be a minimum both second derivatives must be positive.

The above conditions are satisfied by the solution:

$$\sin\theta' = \frac{\sqrt{3}B_0}{\sqrt{A_0^2 + 3B_0^2}} \qquad \cos\theta' = \frac{A_0}{\sqrt{A_0^2 + 3B_0^2}} \qquad U' = \frac{3d}{\sqrt{A_0^2 + 3B_0^2}} \qquad (7.4)$$

Note that this solution is not based on any assumptions or restrictions as to the nature of the correlation field.

If the actual flow angle θ is known independently, as for example from the peak correlations, the minimization can be performed with respect to speed alone, and the solution takes the form.

$$U = \frac{3d}{\left(A_0 \cos\theta + \sqrt{3}B_0 \sin\theta\right)} \qquad (7.5)$$

Replacing the constants $\sqrt{3}B_0$ and A_0 in terms of *sin*θ' and *cos*θ' reduces this equation to the form

$$U = \frac{3d}{\sqrt{A_0^2 + 3B_0^2}} \frac{1}{\cos(\theta' - \theta)}$$

or

$$U = \frac{U'}{\cos(\theta' - \theta)} \qquad (7\,.6)$$

This confirms the result derived earlier in section 6.

<u>The solution in the correlation plane</u>

The information derived from the three cross-correlation functions can be interpreted as sections through a two dimensional correlation field over the x-y plane. The nature of the correlation process imposes a degree of symmetry on the correlation distribution. Which of the pair of time series is chosen as the reference for the correlation determines the direction of the correlation along the line joining the two transducers, ie reversing the choice of reference time series has the effect changing the direction of the correlation by 180 degrees. Defining the coordinate system of the correlation plane x, y as along and normal to the flow direction, the correlation field deduced from the three component array has reflection symmetry under the transformation $\mathrm{x} \to -\mathrm{x}$ and $\mathrm{y} \to -\mathrm{y}$.

The reference transducers for the correlations in ASFM algorithm are chosen to yield positive time delays consistent with the flow direction at each transducer pair. The horizontal and vertical pairs have the upstream transducer as the reference time series, whilst the diagonal cross correlation is referenced to the vertical transducer. The y coordinate is defined with respect to the reference time series of the correlation pair, ie for flow angles in the upper half plane, the cross-correlation function for the horizontal pair represents a section across lower half of the correlation plane, likewise for the diagonal cross-correlation, since the displacement is negative with respect to the vertical transducer. The vertical cross-correlation function cuts across the upper half of the plane. The horizontal position of the correlation peaks in the correlation plane is given by subtracting the geometrical displacement from the flow displacement:

$$\begin{array}{lll} \text{Horizontal} & x = U\Delta T_H - d\cos(\theta) & y = -d\sin(\theta) \\ \text{Vertical} & x = U\Delta T_V - d\cos(60-\theta) & y = d\sin(60-\theta) \\ \text{Diagonal} & x = U\Delta T_D - d\cos(60+\theta) & y = -d\sin(60+\theta) \end{array} \tag{7.7}$$

The symmetry of the correlation process can be exploited to transform the correlation functions on to the upper half plane.

The solutions for the flow speed and angle developed above are now utilized to determine the best fit of the correlation peaks to a radial line in the correlation plane.

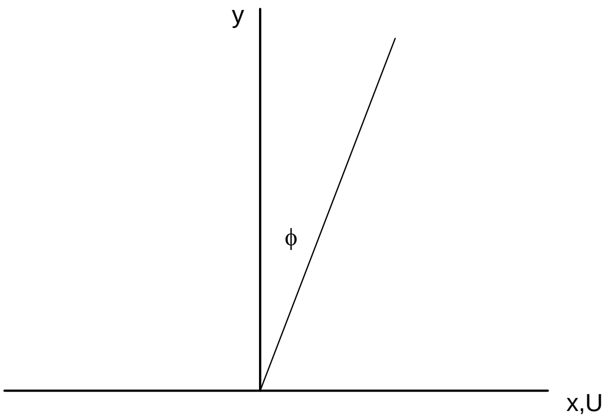

Figure 7.1 The correlation plane.

A least squares fit in the x coordinate is sought assuming that the y coordinates are exact, with the fit is assumed to be of the form,

$$x = y\tan(\phi).$$

Minimizing the residuals about this line yields

$$\tan(\phi) = \frac{\sum xy}{\sum y^2} \tag{7.8}$$

Utilizing the positions of the peaks in the correlation plane given by equations (7.7), the summations of equation (7.8) become

$$\sum xy = \frac{dU}{2}\left[\sqrt{3}B_0\cos(\theta) - A_0\sin(\theta)\right] \qquad \text{and} \qquad \sum y^2 = \frac{3d^2}{2} \tag{7.9}$$

where A_0 and B_0 are as defined earlier in this section.

Replacing the parameters A_0 and B_0 in terms of $\cos(\theta')$ and $\sin(\theta')$, and U in terms of U', reduces the expression for $\sum xy$ to

$$\sum xy = \frac{3d^2}{2}\tan(\theta' - \theta)$$

and hence equation 7.8 yields

$$\tan(\phi) = \tan(\theta' - \theta) \tag{7.11}$$

The difference between the angles derived from the time delays and from the correlation peaks, ϕ_P is thus identified with the best linear fit to the correlation peaks. The results of section 6 are thus confirmed, irrespective of the time delay checksum.

The residuals in the correlation plane

The residuals of the individual contributions to the least squares fit in the correlation plane are given by

Horizontal pair $\qquad \frac{U\Delta T_H}{d} - \cos(\theta) + \sin(\theta)\tan(\phi)$

Vertical pair $\qquad \frac{U\Delta T_V}{d} - \cos(60 - \theta) - \sin(60 - \theta)\tan(\phi)$

Diagonal pair $\qquad \frac{U\Delta T_D}{d} - \cos(60 + \theta) + \sin(60 + \theta)\tan(\phi)$

Writing U as $U'/\cos(\phi)$ for the horizontal pair gives

$$\frac{1}{\cos(\phi)}\left[\frac{U'\Delta T_H}{d} - \cos(\phi)\cos(\theta) + \sin(\phi)\sin(\theta)\right]$$

or,
$$\frac{1}{\cos(\phi)}\left[\frac{U'\Delta T_H}{d} - \cos(\theta')\right]$$

Writing *U'* and cos(*θ'*) in terms of the time delay parameters A_0 and B_0 and simplifying, the residual becomes

$$-\frac{U'(\Delta T_V + \Delta T_D - \Delta T_H)}{3d\cos(\phi)}$$

in terms of the true speed U, $-\dfrac{U(\Delta Y_V + \Delta T_D - \Delta T_H)}{3d}$

ie the magnitude of the residual is one third of the scaled time delay checksum, S. Repeating the calculation for the vertical and diagonal correlation pairs yields similar results.

ie. Horizontal residual = -*S/3*,
Vertical residual = +*S/3* (7.12)
Diagonal residual = +S/3

Each of the residuals is equal in magnitude to one third of the scaled checksum S.

Figure 7.2 shows the positions of the peaks in the correlation plane with normalized coordinates for the case where both the checksum and peak offset angle are positive. The full lines indicate the ordinates of the peaks given by the above solutions, and the dashed lines their transposed counterparts. The dashed curve is the locus of the peaks, the magnitude of their horizontal displacements from the radial line being in all cases S/3.

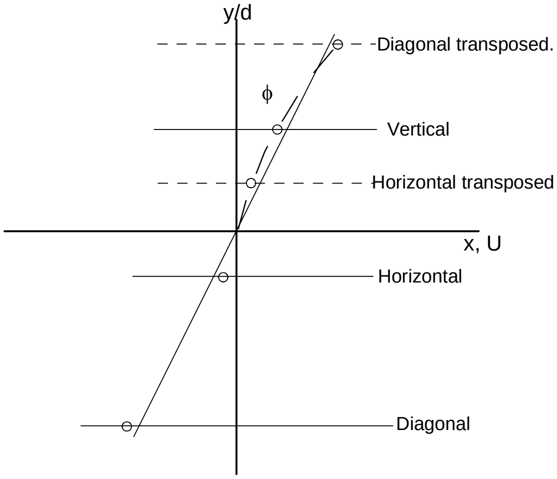

Figure 7.2. The correlation plane for non-zero checksums.

Figure 7.2 is derived from the output of the algorithm and in general is an approximation to the actual physical correlation plane. The calculation of the flow angle θ assumes that the correlation peaks lie on a radial line, ie that the checksum is zero, and for non-zero checksums the flow angle will be slightly in error, introducing small errors in both the x and y coordinates calculated for the peak positions. The main characteristics of the diagram, such as the direction of the offset of the peaks from the normal, and the curved nature their locus are correctly reproduced.

8. The correlation ellipse

Knowing the flow speed and angle, the positions of the cross correlation curves in the correlation plane can be calculated. With the inclusion of the auto-correlation function, this furnishes the correlation distribution along three lines parallel to the flow direction. This provides sufficient information to construct a reasonable representation of the mean correlation field. Figure 8.1 shows an example of such a reconstruction using a numerical contour fitting routine.

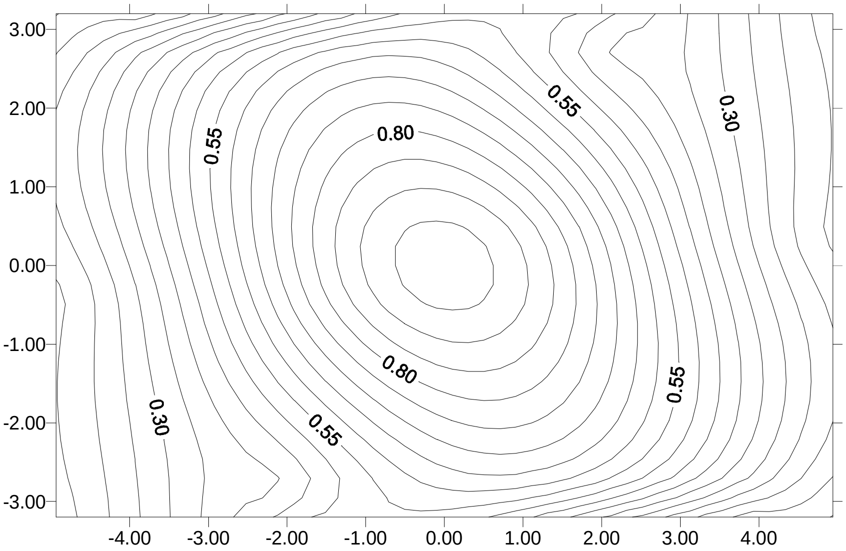

Figure 8.1. The correlation field derived from Wells Unit 3 data.

The contours are elliptical in character, and show the inclination of the ellipse, in this case close to 45^{o}. The peak offset angle is given by the tangent points to the contours parallel to the flow direction, i.e. the horizontal axis of the figure.

The flow angle solutions based on the time delays and the correlation peaks, θ' and θ respectively, together with the correlation scale of the auto-correlation function, are sufficient to furnish an analytical solution for a characteristic correlation ellipse.

The two dimensional correlation function is assumed to have the Gaussian form

$$f(y,\phi) = \exp\left(-\frac{y^2}{\cos^2(\phi)\sigma_o^2 k^2}\right) \tag{8.1}$$

where y is the distance normal to the flow direction, and ϕ the direction coordinate, measured clockwise from the normal. The length scale σ_o is the correlation scale along the major axis of the ellipse, and k is a scaling factor whose value is defined by the ellipse, being 1.0 and β along the major and minor axes respectively. The geometry of the ellipse is defined below in figure 8.2.

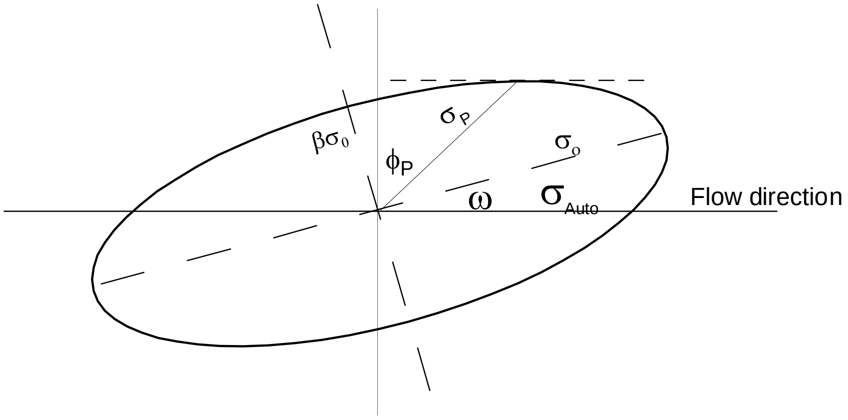

Figure 8.2 Geometry of the fitted anisotropy ellipse.

The length scale along the line of the correlation peaks σ_P and the peak offset angle ϕ_P are known from the solutions for the flow angles θ, and θ'. The length scale in the flow direction, σ_{Auto} is obtained directly from the auto-correlation function. These three quantities are sufficient to define the parameters of the ellipse, and hence determine the eccentricity β, major axis σ_o and the angle of inclination ω. The detailed solution is provided in appendix B.

The correlation length scale factor k is described by the polar form of the ellipse as

$$k^2 = \frac{\beta^2}{\cos^2(\omega+\phi) + \beta^2 \sin^2(\omega+\phi)} \tag{8.2}$$

The exponent of the Gaussian correlation function of equation (8.1) is then

$$-\frac{y^2\left[\cos^2(\omega+\phi) + \beta^2 \sin^2(\omega+\phi)\right]}{\sigma_o^2 \beta^2 \cos^2 \phi} \tag{8.3}$$

The correlation peak occurs when this exponent is a minimum, ie when

$$\tan(\phi) = \frac{(1-\beta^2)\tan\omega}{\beta^2 \tan^2 \omega} = \tan\phi_P \tag{8.4}$$

Figure 8.3 shows the variation of the angle ϕ_P with both β and ω, where the maximum displacement of the peaks occurs at

$$\cos(2\omega) = \frac{(1-\beta^2)}{(1+\beta^2)}$$

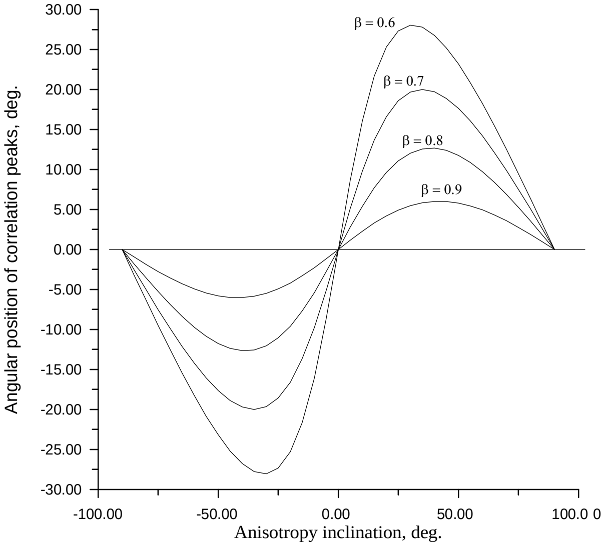

Figure 8.3 Variation of the peak displacement angle ϕ_P with β and ω.

Figures 8.4 (a) and (b) show the distribution of the angle of inclination ω and the eccentricity β for the Kennebec Unit 2 data of figure 5.2. Figure 8.4 (a) shows sketches of the changes in the configuration of the ellipse over the height of the intake.

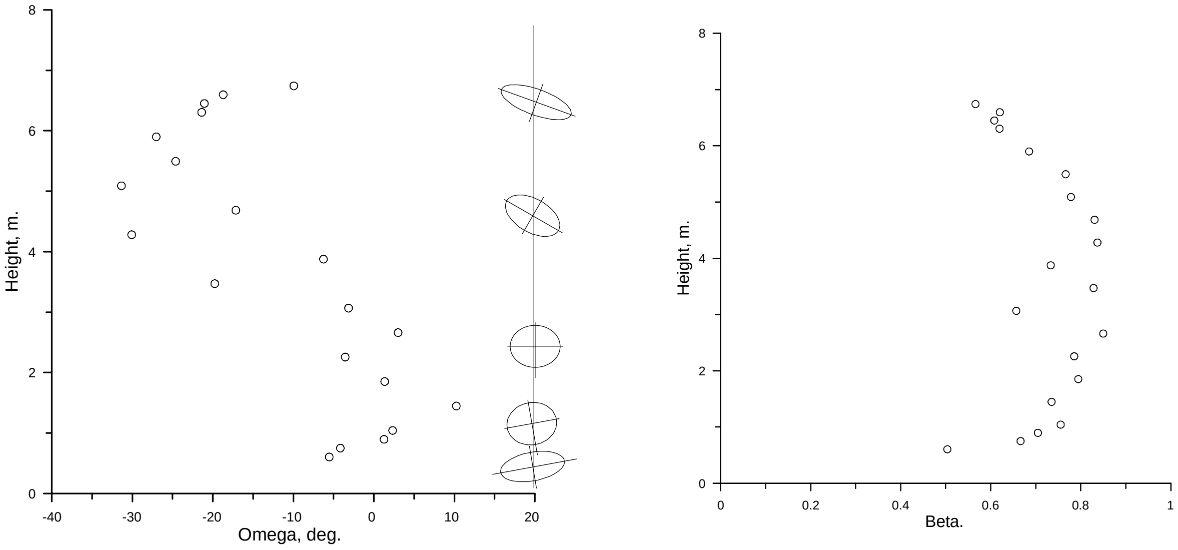

(a)

(b)

Figure 8.4. Kennebec Unit 2, (a) inclination ω, (b) eccentricity β.

9.0 Calculation of cross-correlation functions from the correlation ellipse

Knowing the basic parameters of the ellipse, i.e. the ratio of the major and minor axes, and their angular offset from the flow direction, the assumption that the form of the auto-correlation function is representative of the general correlation field can be applied to calculate the cross correlation functions along the transects defined by the flow direction.

The comparison between the cross-correlations calculated in this way from the output of the algorithm and the original measured values provides a test of the validity of the assumption that the auto-correlation function is representative of the correlation field as a whole.

In view of the anticipated sensitivity of the test, the calculation of the flow angle from the correlation peaks has been based on the measured autocorrelation function instead of the Gaussian profile adopted for the standard algorithm. This now requires a least squares numerical solution for the flow angle θ and the peak correlation scale σ_P. Figure 9.1 illustrates a typical correlation field found in practice, with the x axis in the flow direction. The ellipse marks a fixed correlation contour, and the dotted line a typical section traced by an ASFM transducer. From the flow angle and the speed, the correlation values along the dotted section can be related to the times of the measured values.

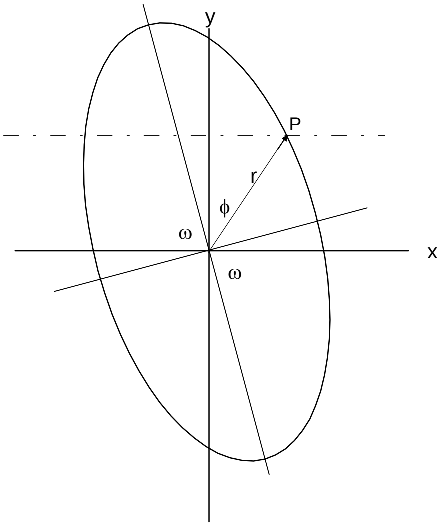

Figure 9.1. The elliptical form of the correlation field.

The correlation function is defined along the radial line r, in the general direction ϕ, with the length scale σ. The radial distribution of the correlation function $f_n(r/\sigma)$ is calculated from a polynomial representation of the shape of the auto-correlation function. As the point P traverses the dotted line, the corresponding cross correlation function is mapped. This has been applied to two data sets, Kootenay Canal, level 5, flow angle -10° and CNR, level 6, flow angle -33°, and the results of the calculation compared with the measured cross-correlation curves. The data sets selected for analysis have been chosen from those with low checksum values to provide an unbiased test of the fundamental model of the correlation field. The data from the CNR plant is an example where the vertical cross correlation peak is close to the limit of detection.

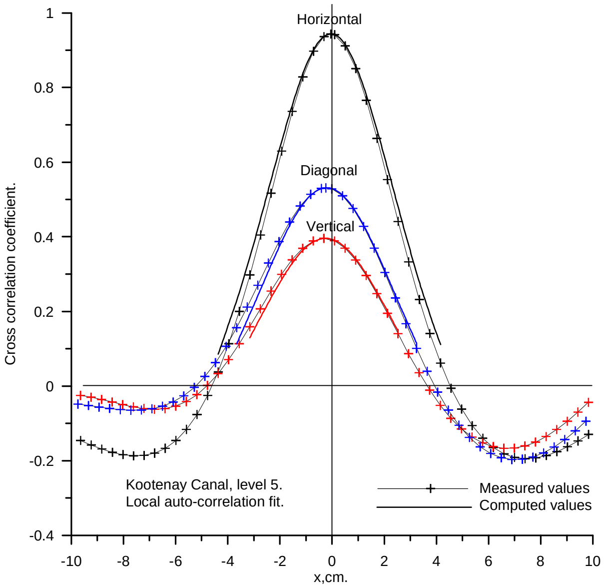

Figure 9.2. Kootenay Canal cross correlations based on the local auto correlation function.

The measured cross correlation functions are constructed from the full length time series, and the flow parameters have been derived from the corresponding correlation peaks and time delays.

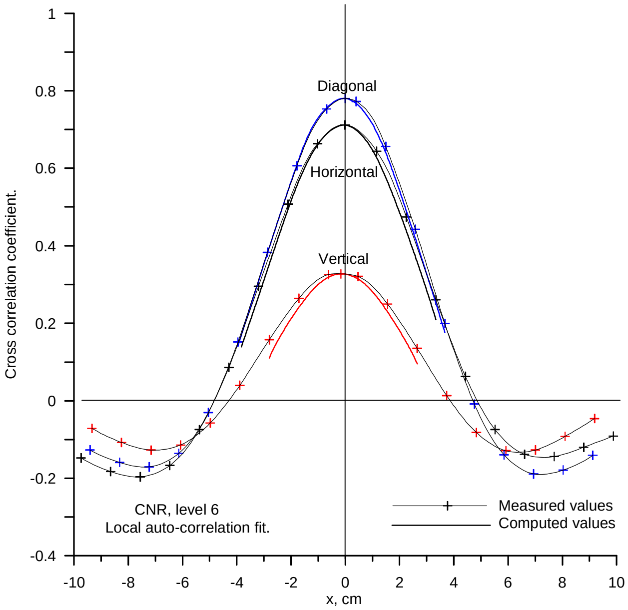

Figure 9.3. CNR cross correlations based on the local auto correlation function.

The Kootenay Canal data set has a scaled checksum value of 0.01, sufficiently low to justify the assumption of the angle calculation that the peaks lie on a radial line, while that for CNR although somewhat greater at 0.03, is still small enough for the radial assumption to hold. The correlation peaks in the figures have been aligned to the zero of the x-axis for ease of comparison.

The match between the calculated and measured cross correlation curves is excellent for both the examples shown, strengthening the case for basing the calculation of the flow angle from the correlation peaks on the form of the auto-correlation function. The CNR data has a flow angle of -33^o and the wide separation of the vertical pair of transducers normal to the flow results in a relatively low value of the vertical correlation peak. This case is thus a more severe test of the model, the correlation peak of 0.3 approaching the lowest level that can be unambiguously detected by the ASFM.

10.0 The selection of the spectral range of the time series cut-off filters.

The analysis of ASFM data collected at a wide variety of hydro-electric plants allows some conclusions to be drawn as to the general characteristics of the turbulence encountered at the measurement plane, and their relevance to the accuracy of the ASFM algorithm. The turbulence sensed by the ASFM consists of a series of interacting wakes generated by the structural members of the trashrack, superimposed on the finer scale turbulence generated by the fine bars of the trashrack itself. This complex mix is typically sampled by the ASFM at distances ranging between 3 m and 20 m downstream of the trashrack, depending on the design of the intake and trashrack.

Of particular relevance to the analysis of the scintillation data is the sensitivity of the derived flow speed and angle to the bandwidth of the filters applied to the time series data. The choice of filter parameters must be optimized to produce consistent results over a wide range of discharge rates. Central to this problem is the degree to which the spectrum of the turbulence can be scaled.

Wygnanski et al (1986) demonstrate the scaling of the spectrum of the turbulent wake far downstream of a horizontal flat plate in an unconstrained flow, where turbulent eddies increase in scale as the flow progresses downstream with an accompanying increase in width, Figures 10.1 and 10.2.

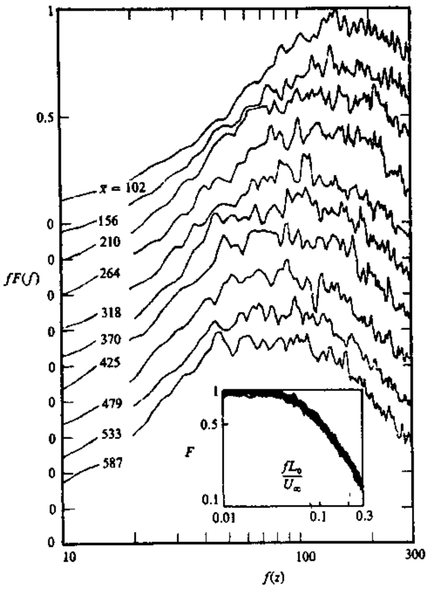

FIGURE 12. Spectra of u fluctuations on centreline of flat-plate wake at various downstream positions. Insert shows similarity of spectra when scaled by L_0 and U_∞.

Figure 10.1. Scaling of centre-line spectra, after Wygnanski et al (1986).

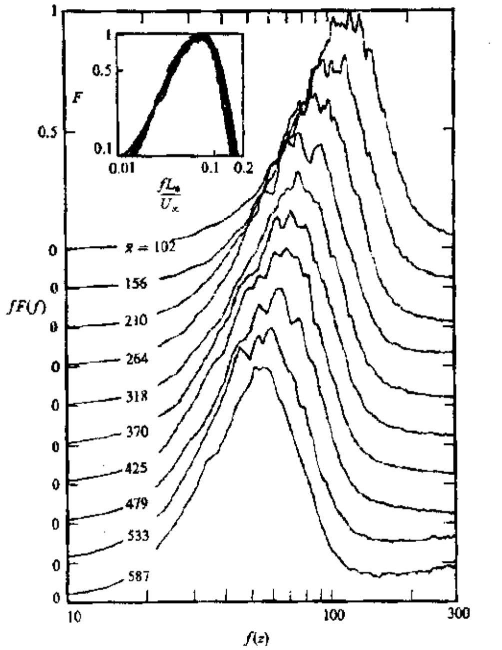

FIGURE 13. Spectra of induced u fluctuations at $\eta = 3$ in the flat-plate wake at various downstream locations. Insert shows similarity of spectra when scaled by L_0 and U_∞.

Figure 10.2. Scaling of off-centre-line spectra, after Wygnanski et al (1986).

The abscissa of the small inset graphs in figures 6.1 and 6.2 are the normalized frequency,

$$\hat{f} = fL_o / U_o \qquad (10.1)$$

where the characteristic length *Lo* and speed U_o are the local width of the wake for each of the spectra and the free stream velocity respectively. This scaling of the frequency has collapsed the many separate spectra to a single curve.

Equation 10.1 represents a normalized wavenumber,

$$\widehat{k} = kL_o$$

Note that this scaling is not limited to the inertial subrange of the spectrum as is assumed in the derivation of the covariance integral, equation 2.1.

The complete scaling of the simple wake cannot be expected to apply to the complex and often rapidly developing flows typical of hydro-intakes. However, in a given intake where the ASFM measurement plane is at a fixed distance downstream, a limited degree of scaling is possible. In many ASFM data sets, the velocity and turbulent kinetic energy profiles scale with the discharge rate, in the case of the latter, the path average of the turbulent kinetic energy along the acoustic beam is proportional to the variance of the acoustic scintillations, and the following scaling is appropriate,

Mean velocity profile $\hat{U} = \dfrac{U}{Q/A}$

Scintillation variance $\hat{\sigma}^2 = \dfrac{\sigma^2}{(Q/A)^2}$

where Q is the total volume flow and A the cross section at the measurement plane. The vertical profiles of $\widehat{U}$ and $\widehat{\sigma}^2$ are then the same for all discharge values.

This scaling has been approximately confirmed for a large number of intakes, the velocity and variance profiles at the different flow rates collapsing to very similar curves. An additional indication of the validity of this scaling is that the flow angles derived from the scintillation data are also largely independent of the flow rate.

From the point of view of the ASFM algorithm based on the interpretation of the cross-correlations of the three acoustic beams, the essential issue is the scaling of the turbulent spectrum in the frequency range accessible to the ASFM. For a given plant, the measurement plane is a fixed distance from the trashrack, and the scaling of the spectra reduces to the matching of the wavenumber range. When filters suitably matched to the flow speed are applied, the scales of eddies sensed by the ASFM are then largely independent of the flow speed.

An example of the effect of filter selection on the peak correlation values is now demonstrated for the 2007 Wells Unit 2 data set. The Wells plant data has been selected here as an example where the measurement plane is close to the trashrack, providing a relatively severe test of the scaling. The flow conditions corresponding to 27% and 99.8% blade angles provide an approximate doubling of the flow speeds. The data has been treated with a range of low frequency cutoff filters, and figures 10.3 and 10.4 compare the variation of the correlation peaks at two levels in terms of both frequency and wavenumber. The data shown has been processed as 2048 point time series, and the results shown on the graphs are the average of a total of four 30 second data runs.

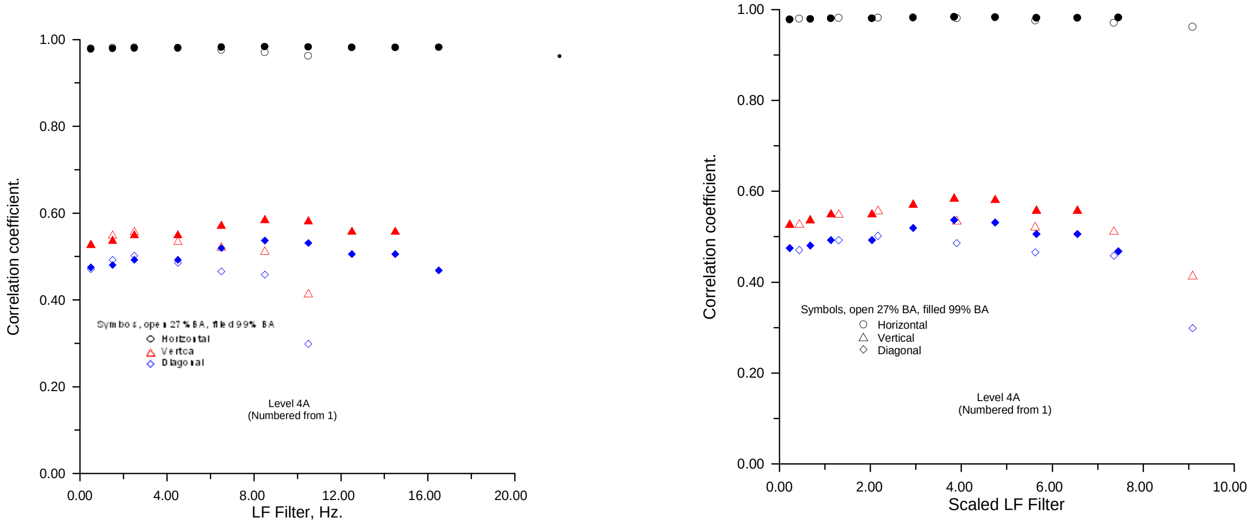

(a) (b)

Figure 10.3. Wells Unit 2, 2007 Level 4. Correlation peaks. a, frequency. b, wavenumber

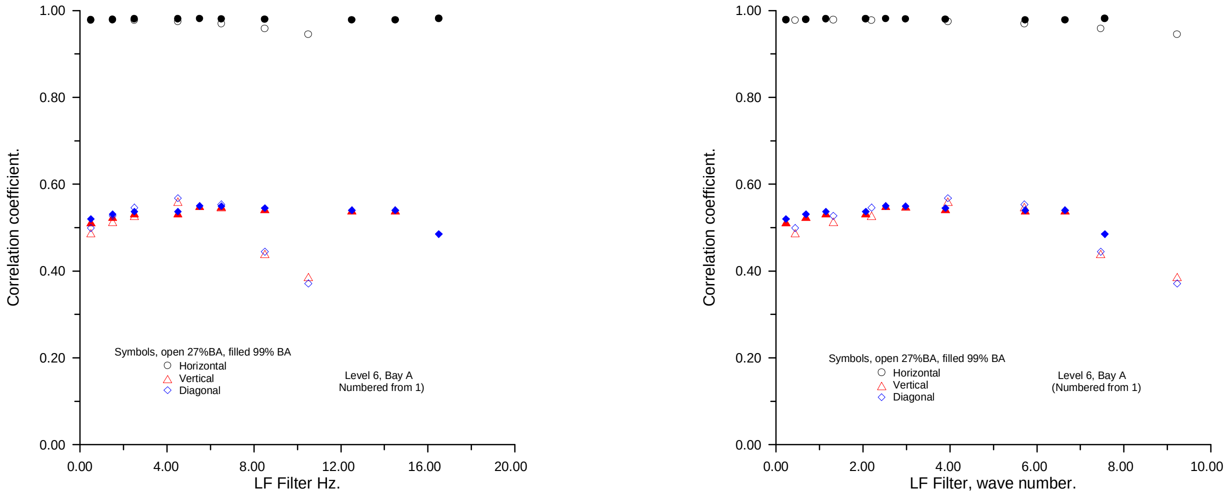

(a) (b)

Figure 10.4. Wells Unit 2, 2007 Level 6. Correlation peaks. a, frequency. b, wavenumber.

When viewed in terms of frequency, the variation of the correlation peaks differs for the two speeds, the peaks falling off more rapidly at higher cutoff frequencies at the lower speed. When viewed in terms of wavenumber, where the filter value is scaled inversely with flow speed, the cross-correlation peak values at the two flow speeds are almost coincident. For both levels shown the flow direction is almost parallel to the horizontal pair.

When the filters are selected such that the wavenumber range is the same at all flow speeds, the correlation peak values are then independent of the flow speed. This is of particular importance for the calculation of the flow angle, where the ratio of the correlation peaks plays an essential role. It is clear from the above figures that if the filters are not adjusted to match the flow speed, the ratios of the peaks may differ, introducing a spurious dependence of flow angle on flow speed.

In operation, the instrument optimizes the high and low pass filters within a fixed wavenumber range, their values being scaled appropriately with the flow speed. The final choice of wavenumber range optimizes the quality of the data selected for analysis. The details of the selection procedure are outlined in appendix C.

11.0 Non-zero time delay checksums

The solution for the flow angle is based on the assumption that the time delay checksum is zero. The observed values of the checksum however, are frequently not negligible, up to the order of 10% of the transit time across the array, significantly greater than the precision of the correlation peak positions themselves. Examination of many data sets establishes that these inconsistencies in the time delays are not random but have a large systematic component, which are an inherent characteristic of the turbulence. Figure 11.1 shows examples of the vertical profile of the scaled checksum taken from the Lower Granite plant (without the fish screens fitted). The time series for this data have been filtered such that the wavenumber range is the same for both flow rates. Note the close correspondence between the profiles from the two flow rates and between all three bays. This strongly suggests that the mismatch in the time delays is systematically related to the properties of the turbulence, and is not the result of random errors.

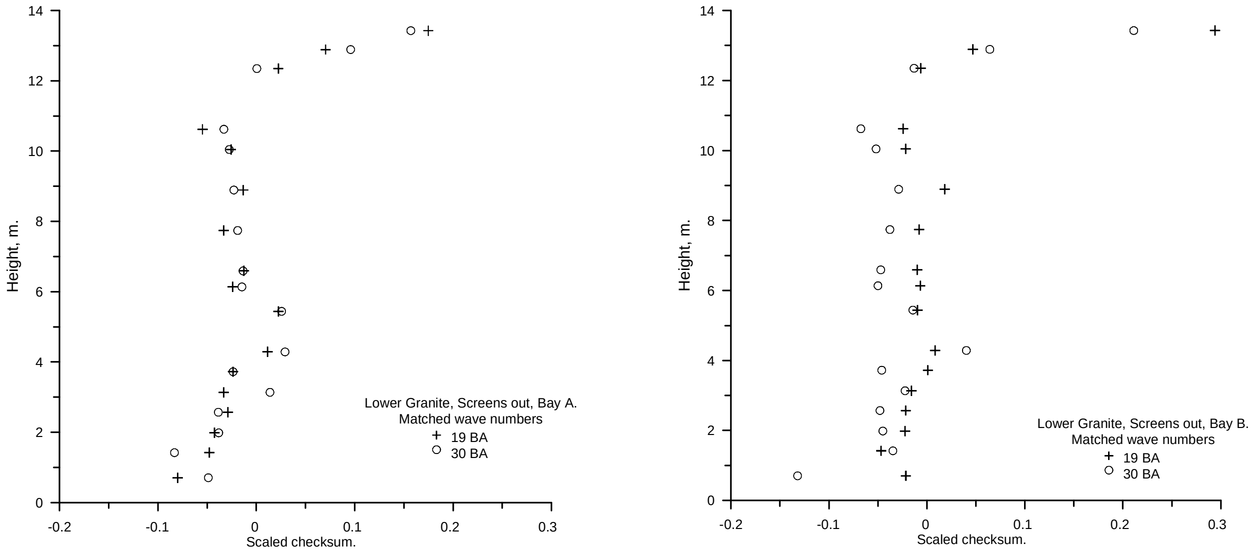

(a) (b)

Figure 11.1. Lower Granite, profiles of scaled checksum, (a) Bay A, (b) Bay B, (c) Bay C.

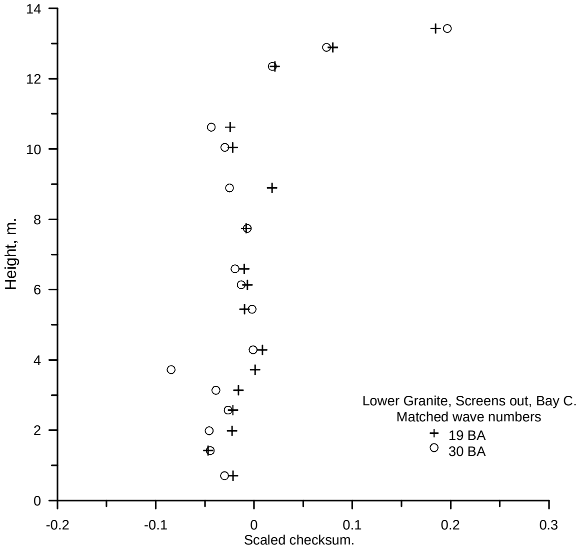

(c)

Further evidence for this systematic behaviour is to be found in the strong correlation between the scaled checksum and the peak correlation offset angle ϕ_P, some typical examples being shown in figures 11.2 to 11.6.

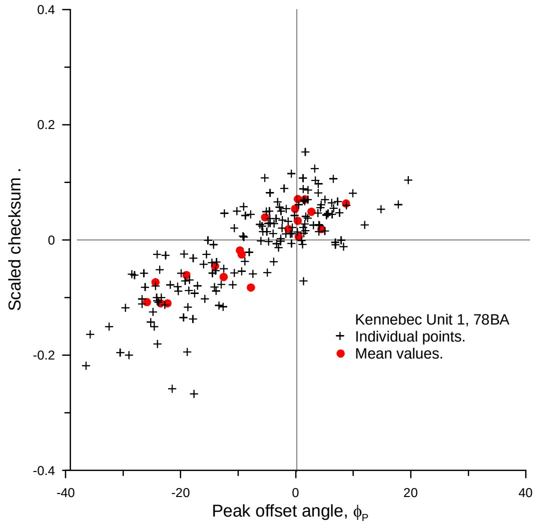

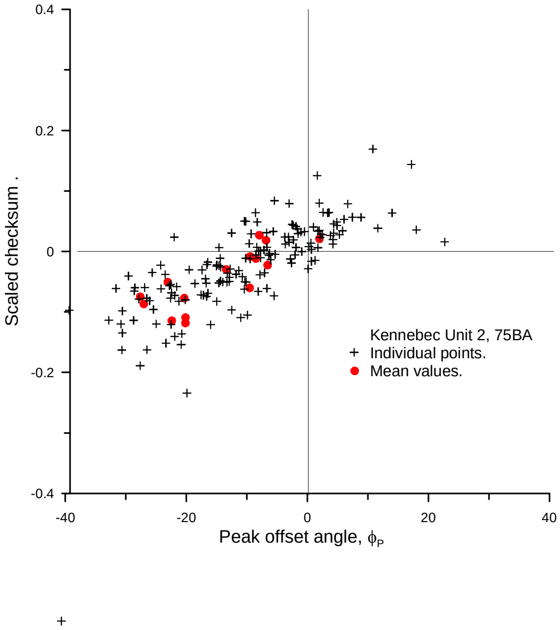

Figure 11.2. Kennebec Unit 1.

Figure 11.3 Kennebec Unit 2.

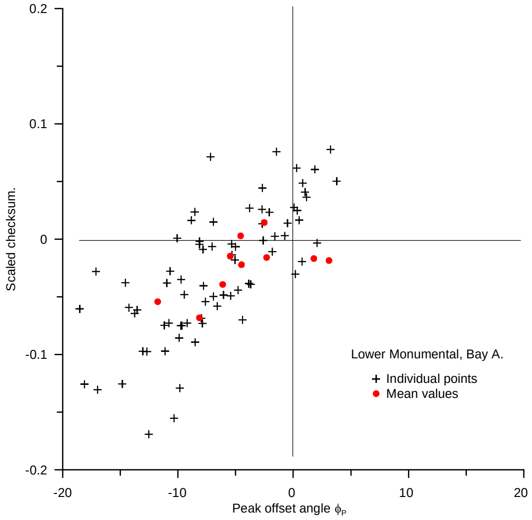

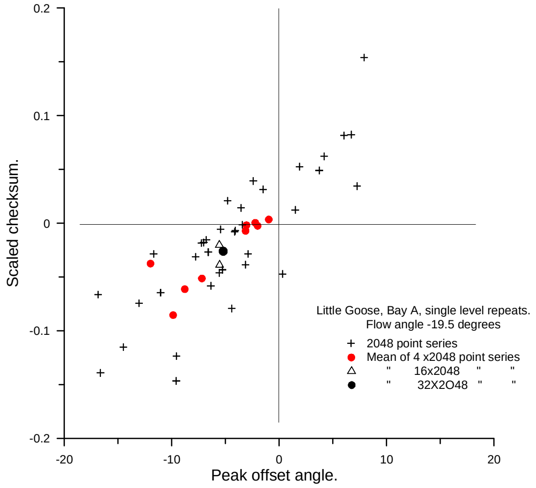

Figure 11.4. Lower Monumental.

Figure 11.5. Little Goose, flow angle =-19.5^{o}

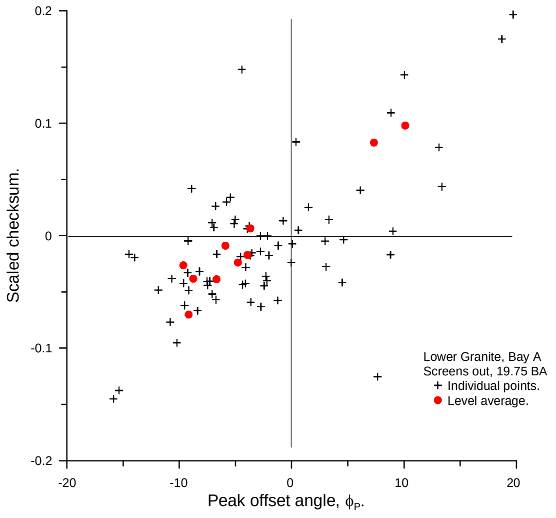

Figure 11.6. Lower Granite, screens out.

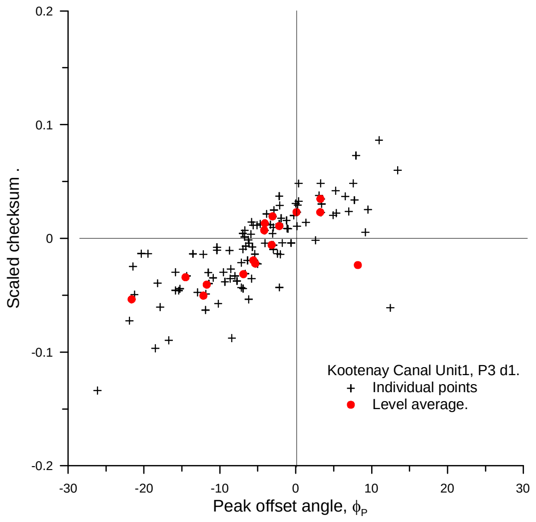

Figure 11.7 Kootenay Canal

The data marked by black crosses are the individual 2048 point segments of time series, with points marking the average for each level shown in red. The figures for the Kennebec, Lower Granite and Lower Monumental plants contain data from all levels and hence encompass a range of flow angles; those for Little Goose on the other hand, are from extended tests at a single level, and have a fixed flow angle of about 19.5^o. In this case the red points are averages of four sets of 2048 point segments, chosen to match the number of points in the averages for each level of the other graphs. The 4x2048 averages marked by the triangles are equivalent of 2 minute average data runs, and the solid black symbol represents 4 minutes of data. The decrease in scatter as the averaging period increases is indicative of the approach of the correlations to statistical stability. Under normal test conditions the outputs of the scintillation system are based on the equivalent of 2 minute averages.

The checksum, although indicating a measure of inconsistency in the time delays, is not of itself a reliable as a direct measure of the quality of the data. To explore the connection between the scaled checksum and the peak offset angle further, the characteristics of the locus of the correlation peaks in the correlation plane have been examined. The locus can be calculated from the flow speed and direction. The calculation is subject to very minor uncertainties due to the inclusion of small errors in the speed and direction arising from the non-zero checksums. However, the calculations are felt to be sufficient to delineate the broad features of the locus. The coordinates of the three correlation peaks transposed into the upper half plane are as follows.

Horizontal pair.

$$\text{For positive flow angles:}\quad x_H = -\left[U\Delta T_H - d\cos(\theta)\right],\quad y_H = d\sin(\theta)$$

$$\text{For negative flow angles:}\quad x_H = \left[U\Delta T_H - d\cos(\theta)\right],\quad y_H = -d\sin(\theta) \qquad (11.1)$$

Vertical pair.

$$x_V = U\Delta T_V - d\cos(60-\theta),\quad y_V = d\sin(60-\theta) \qquad (11.2)$$

Diagonal pair.

$$x_D = -\left[U\Delta T_D - d\cos(60+\theta)\right], \quad y_D = d\sin(60+\theta) \quad (11.3)$$

The degree of departure of the locus of the correlation peaks from a radial line was show in section 7 to be directly related to the scaled checksum. The locus can be classified into four characteristic forms, shown in figure 11.8 below. The characteristics of the turbulence field determine which of the four possible forms is observed; as is illustrated by the consistent relationship between the peak offset angle and the scaled checksum for typical ASFM data,.

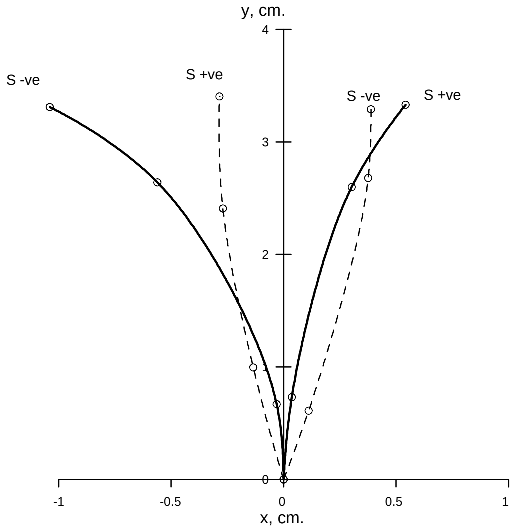

Figure 11.8 Most common correlation peak locus forms.

The loci illustrated in figure 11.8 are associated with the quadrants of the peak offset-scaled checksum plots, shown below, figure 11.9 for flow angles between 0^o and -60^o. The sign of the checksum reverses at 60^o intervals of the flow angle as the correlation pairs cyclically interchange.

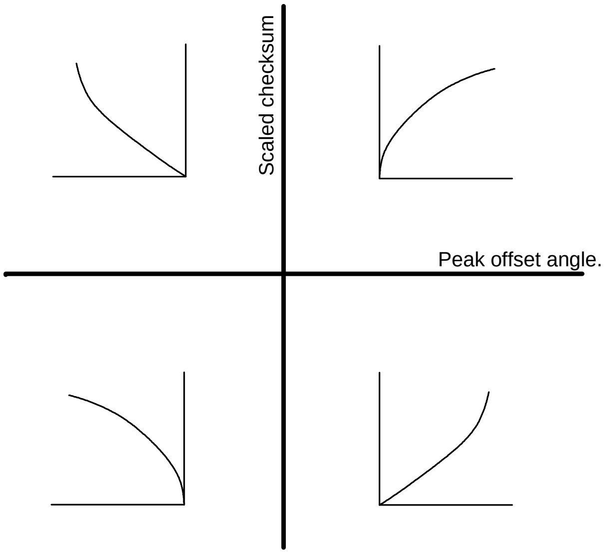

Figure 11.9. Configuration map for the correlation peak locii.

The relationship between the scaled checksum and the systematic error in flow angle derives from two separate effects. The underlying factor is the form of the locus of the correlation peaks, a characteristic of the turbulence itself. Superimposed on this is the effect of the alignment of the transducer array relative to the flow direction. Referring to figure 11.8, the positions of the correlation peaks are marked by circles, and the alignment of the transducer determines the points where the locus is sampled, and hence the value of the checksum. The closer to the origin the peaks are grouped, the lower the checksum, and the most accurate the flow angle calculation. For a given form of peak locus, there is a well defined relationship between the transducer array alignment and the checksum and the flow angle error.

For detailed analysis, the locus is more conveniently expressed in terms of the tangent of the peak offset angle, figure 11.10, showing the case with negative peak offset angles.

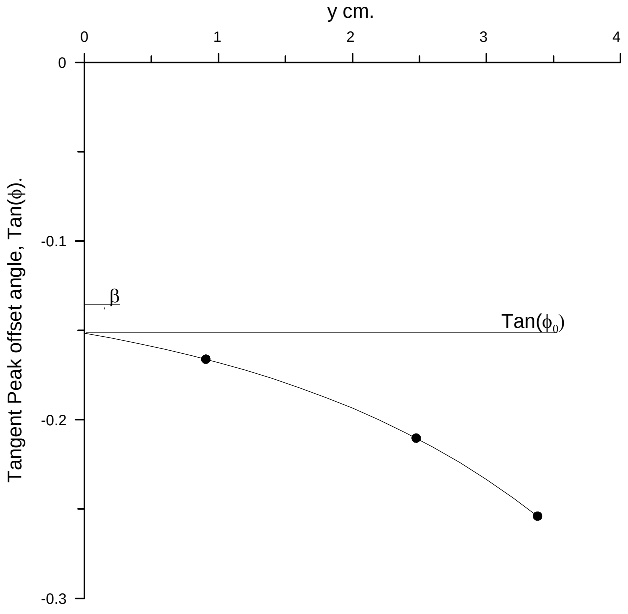

Figure 11.10. Correlation peak locus, tangent form.

Within limits, the locus now is well described by an exponential fit,

$$\tan(\phi) - \tan(\phi_0) = \beta\left[\exp(ny) - 1\right] \tag{11.4}$$

The three correlation pairs furnish three equations of the form of (11.4), eliminating the factor [*Tan*(ϕ_0)-β], the following equation in the exponent *n* is obtained.

$$\frac{\exp(ny_H) - \exp(ny_D)}{\exp(ny_H) - \exp(ny_V)} = \frac{\tan(\phi_H) - \tan(\phi_D)}{\tan(\phi_H) - \tan(\phi_V)} \tag{11.5}$$

This can be solved numerically for the exponent n, and hence the factors β and $Tan(\phi_0)$ can be obtained.

The definition of the locus based on only three points raises the question of the sensitivity of the derived locus to the position of the sample points, as this is determined by the orientation of the acoustic array. As a sensitivity test, the flow solution and correlation peak locus derived from a particular level has been used to back-calculate the time delays and correlation peak values. The calculation has then been repeated for the same locus and flow speed, but with a range of array orientations relative to the intake horizontal. It is found that there is considerable variation in the values of the fitting parameters as the array orientation is changed; however, the actual loci defined by the different fits are almost identical. The following graphs show an example taken from the Kennebec Unit 2 data set of figure 11.3, the original data point is marked in red.

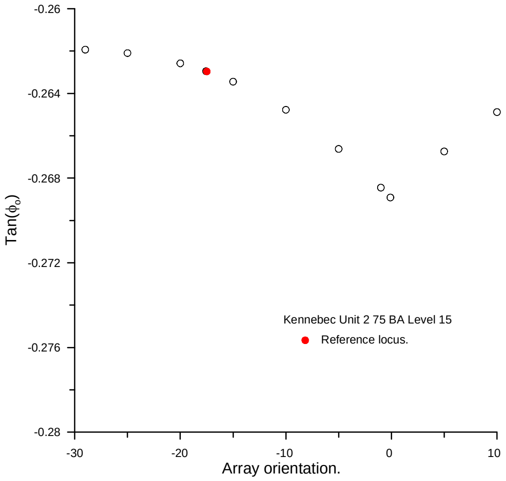

Figure 11.11. Tan(ϕ_o) sensitivity.

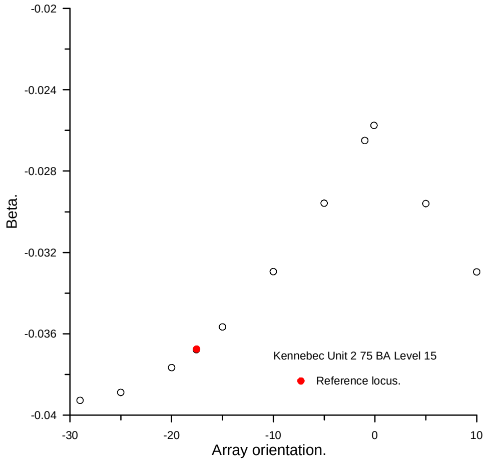

Figure 11.12. Beta sensitivity.

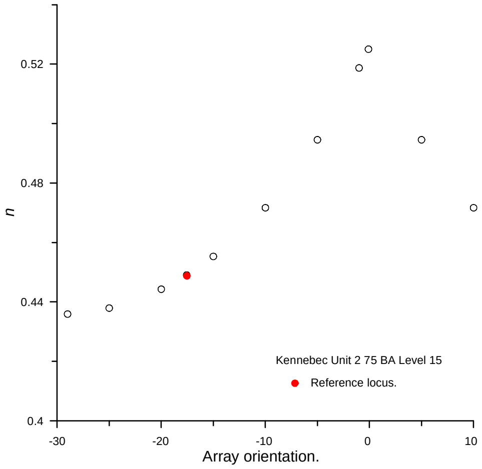

Figure 11.13. Exponent n sensitivity

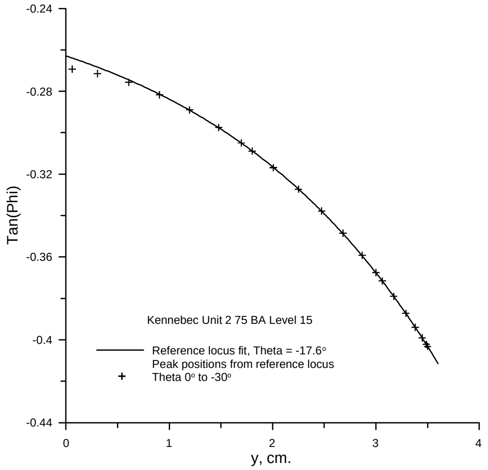

Figure 11.14. Multiple fits to locus.

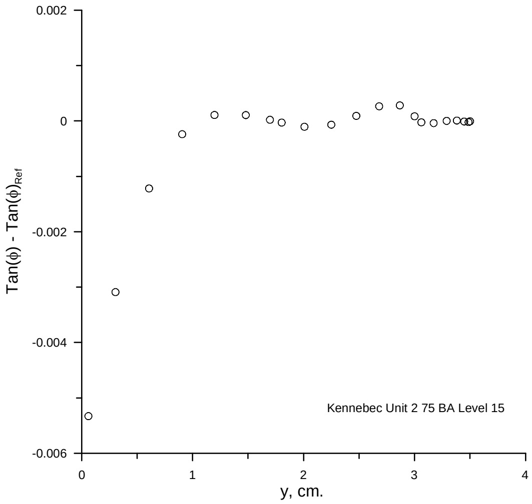

Figure 11.15. Variation in locus due to array orientation.

The form of the locus is, for all practical purposes, uniquely defined by fitting parameters returned from a wide range of array orientations, although the parameters themselves may vary widely.

Since the set of equations is fully determined, a solution can always be found, although in some cases, the resulting loci are physically unrealistic. The physically acceptable solutions are restricted to monotonically increasing or decreasing values of both the x-coordinate and $Tan(\phi)$. Many of the points excluded are those with low checksum and correlation peak offset angles, where all three peaks have small offsets from the y-axis, which are probably random in nature and the errors in flow angle are expected to be negligible. At the other extreme are cases where the scaled checksums are excessive, often combined with large peak offset angles and irregular peak distributions. In these large checksum cases the correlations are often of poor quality, and usually occur in regions of separated flow. Between these two extremes, where the correlation peak loci are physically acceptable, the systematic errors arising from the curvature can be estimated.

The characteristics of the correlation peak locus have been examined for a number of examples, two of which represent more challenging conditions, Kennebec Unit 2 and the Lower Granite plant when fitted with fish screens, and two cases where a direct comparison with other measurement systems is available, Kootenay Canal (Almquist et al. 2011), and the Lower Granite plant without the fish screens deployed, (Wittinger 2005). The figures for these four plants display results from multiple levels with different flow angles. For the Lower Granite (without fish screens) and Kootenay Canal tests the agreement between the measurement systems was within 1%. The Little Goose data of figure 11.5 provides a contrasting case of a single level and fixed array orientation relative to the mean flow.

The following figures show the relationship between the correlation peak offset and the scaled checksum for the mean values at each level, but distinguish between levels where the correlation peak locus fits are acceptable and those which are rejected due to irregular peak distributions.

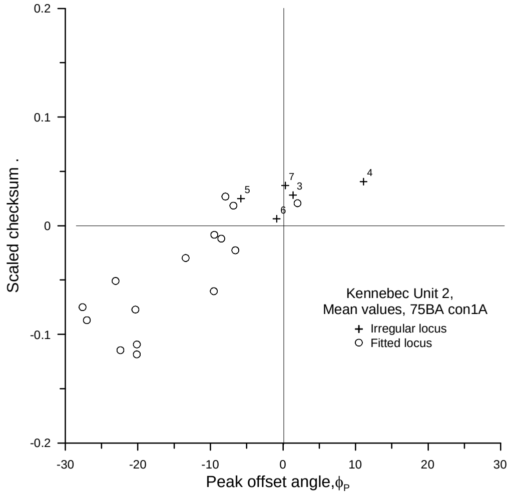

Figure 11.16. Kennebec Unit 2.

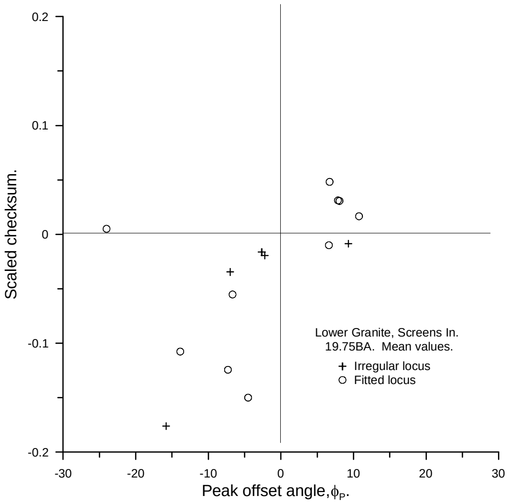

Figure 11.17. Lower Granite, Screens in.

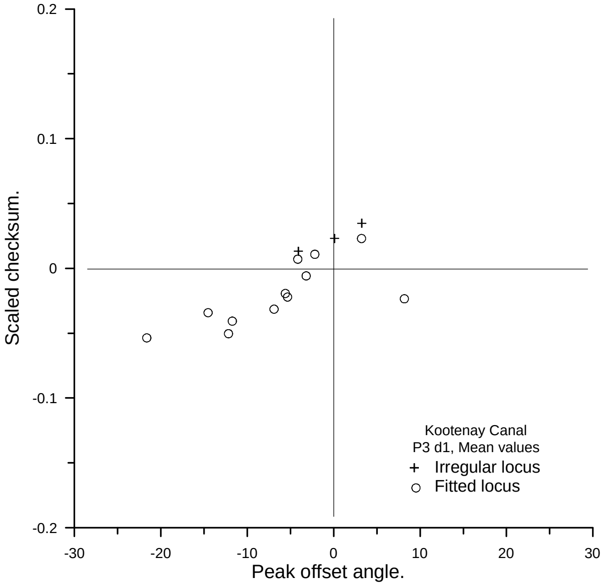

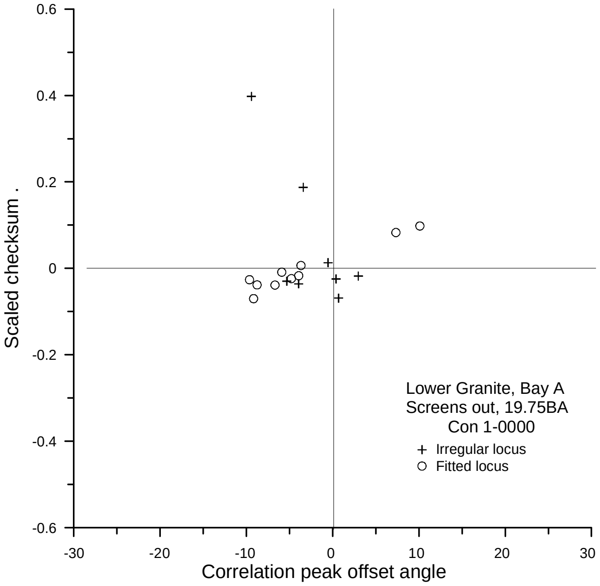

Figure 11.18. Kootenay Canal.

Figure 11.19. Lower Granite, without Screens.

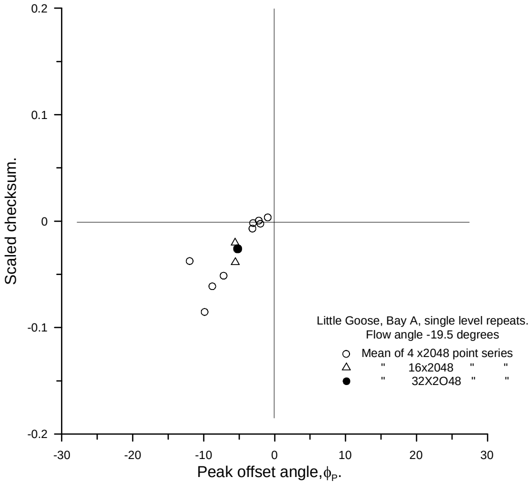

Figure 11.20. Little Goose, single level.

The majority of the cases where the locus is identified as being irregular lie between +/- 10^{o} correlation peak offset angles and scaled checksum values of +/- 0.05, and in this range, points where the errors can be estimated, they are found to be negligible. On this basis, the irregular points in this range are judged to be negligible. At the other extreme, there are a few cases where both peak offset angle the scaled checksums are large, and these usually occur in regions of flow separation, such as near the roof. Thus it is usually possible to estimate the systematic errors in flow angle over most of the measurement plane. Note the comparatively small degree of scatter for the single level for the Little Goose data. The majority of the data lies in the third quadrant of the above plots, identifying the locus as having a negative correlation peak offset angle, combined with a positive curvature. This form appears to be characteristic of the turbulence for most of the plants so far tested.

As the fitting parameters for the locus reflect both the turbulence characteristics and the flow angle, they are not presented here, except to note that $Tan(\phi_o)$ and Beta reflect the peak offset angle and the scaled checksum respectively, whilst the exponent n correlates with the array orientation. As shown previously, the locus defined by a particular set of parameters is essentially unique, and can be used as the basis for the estimation of the systematic errors arising from the non-zero checksums.

12.0 Calculation of the systematic errors due to non-zero checksums

The solution for the flow angle of Section 5 is extended to the non-zero checksum case by defining the distribution of the correlation function in terms of the distance *s* along the locus of the correlation peaks. The solution of assuming that the locus is a radial line is taken as a sufficient good first order approximation to define the correlation peak locus, as demonstrated in the previous section.

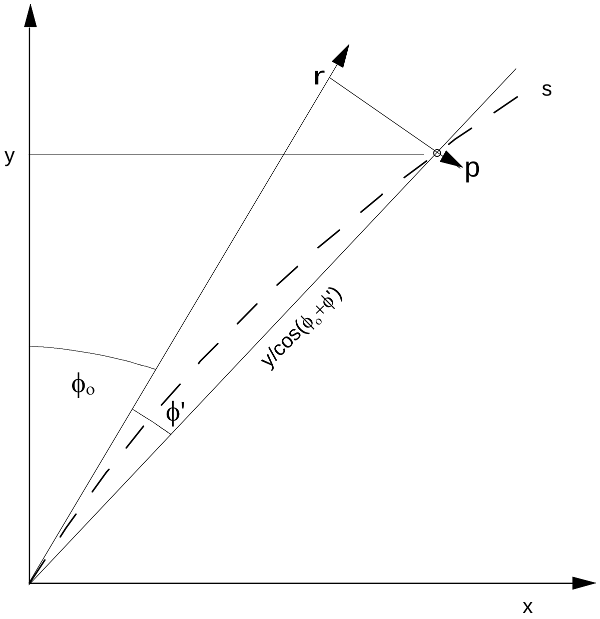

Figure 12.1. Definition of coordinate system for non-zero checksum solution.

The individual offset angles are expressed in the form.

$$\phi = \phi_o + \phi'$$

where ϕ_o is the tangent to the locus at the origin, ie the offset identified in equation 11.4 with the exponential fit to the locus, with ϕ' taken to be small in comparison. The integration to determine the distance *s* is given in terms of the *r*, *p* coordinate system defined in figure 12.1 as,

$$s = \int_0^r \left[1 + (dp/dr)^2\right]^{1/2} dr \tag{12.1}$$

Under the assumption that the terms involving $\tan(\phi')$ are small,

$$s = r + \frac{1}{2\cos(\phi_0)}\int_0^y \left[\frac{dy\tan(\phi')}{dy}\right]^2 dy \qquad (12.2)$$

The exponential fit to the locus then provides the required relation between $\tan(\phi')$ and *y*, to enable the integral to be evaluated to give the following expression for *s*

$$s = r + \frac{\beta^2}{2\cos(\phi_0)}\left\{\frac{e^{2ny}[2ny(ny+1]-1}{4n} - y(2e^{ny}-1)\right\} \qquad (12.3)$$

i.e. the radial distance of the first order solution plus a small correction term.

The error arising from the assumption that the terms in $\tan(\phi')$ are small amount at most to 10% of the correction for curvature, with 2% as a more typical value, estimated by calculating the magnitude of the complete terms and comparing them with the approximated equivalents.

The correlation function is then taken in the from

$$f = a\exp(k^2 s^2)$$

The three correlation peaks are then specified by the flow angle θ, the wavenumber *k* and the coefficient *a*. These are then adjusted in a minimum least squares routine based on the difference between the measured and calculated correlation peaks. The corrected flow angle is then used to re-calculate the flow speed. The difference between the output of the standard algorithm and the calculation taking into account the curvature of the locus is regarded a measure of the systematic error.

Figures 12.2 to 12.5 show the relation between the error estimates and the correlation peak offset angles. The equivalent plots for the scaled checksum, figures 11.16 to 11.19, show that most of the levels where the correlation peak distributions are inappropriate for fitting lie in the ranges of +/ 10^{o} for peak offset angle and +/- 0.05 in scaled checksum. In this peak offset angle range, the error plots of figures 12.2 to 12.5 show that for scaled checksums less than +/- 0.1 the errors are negligible. Apart from two instances for the Lower Granite plant where the fish screens are fitted, the systematic errors are less than 0.5^{o} in flow angle, and 0.5% in speed.

Figures 12.6 to 12.9 show the corresponding height distributions of the systematic errors. Two features are worthy of note. The distribution pattern of the errors for the Kennebec data show a group of three points near the roof to be displaced from the main trend. The arrays at these levels are oriented at 90^{o} to the rest of the set, and illustrate the effect of array orientation on the systematic errors. Likewise the scaled checksums are elevated for these levels. The lower three arrays are also oriented at 90^{o} and have correspondingly higher checksums, but as the correlation peak offset angles are small, the systematic flow angle errors remain low.

The Lower Granite data with the fish diversion screens deployed, figure 12.7 has a peak in the errors at 10m which is mirrored in the scaled checksum. This is probably associated with the structural supporting members of the fish screen. Only in the conditions of extreme flow disturbance with the fish diversion screens deployed do the systematic errors exceed 1^{o} and 1%.flow respectively for the flow angle and speed.

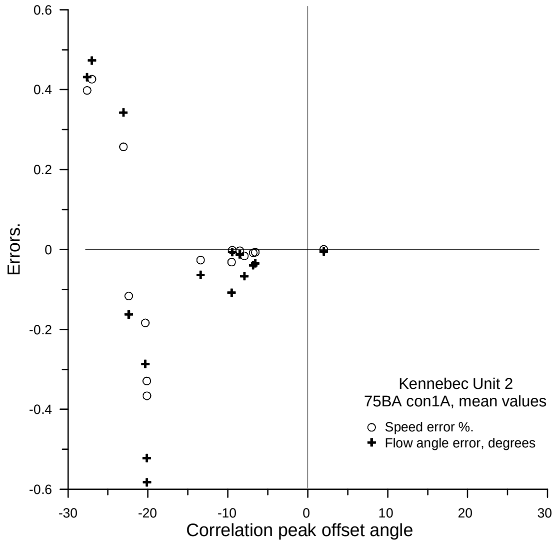

12.2. Kennebec Unit 2, errors

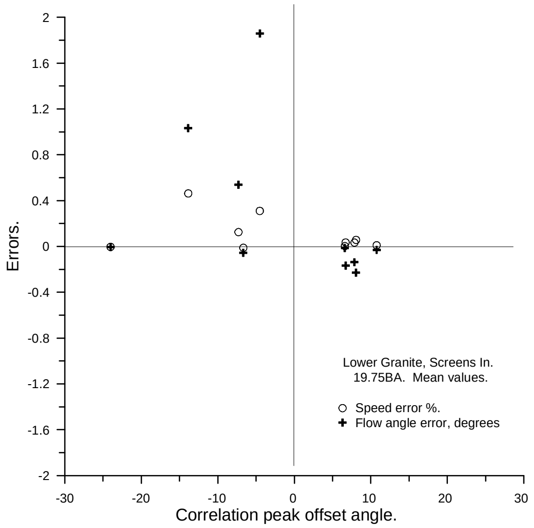

Figure 12.3. Lower Granite, screens in, errors.

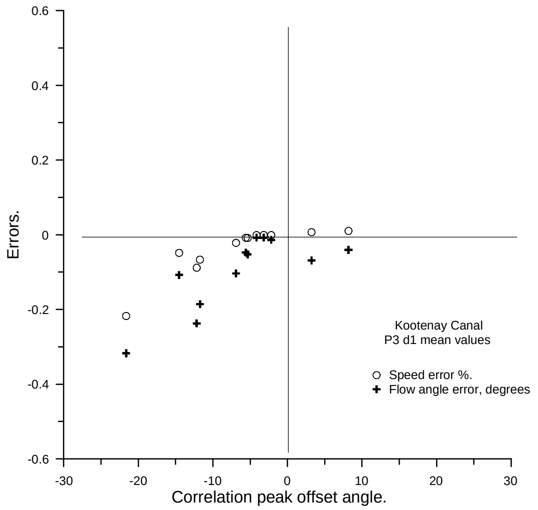

Figure 12.4 Kootenay Canal, errors

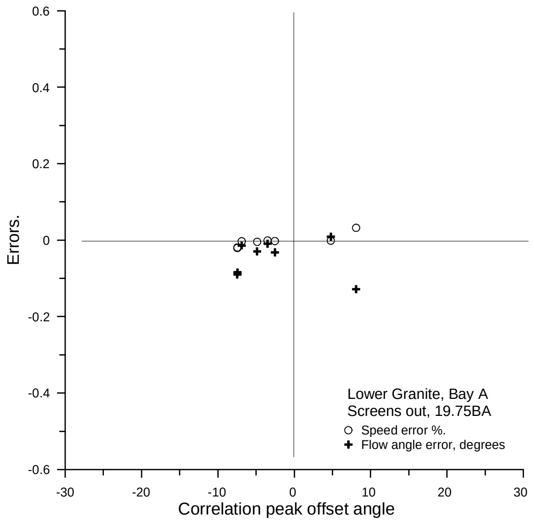

Figure 12.5. Lower Granite, screens out, errors.

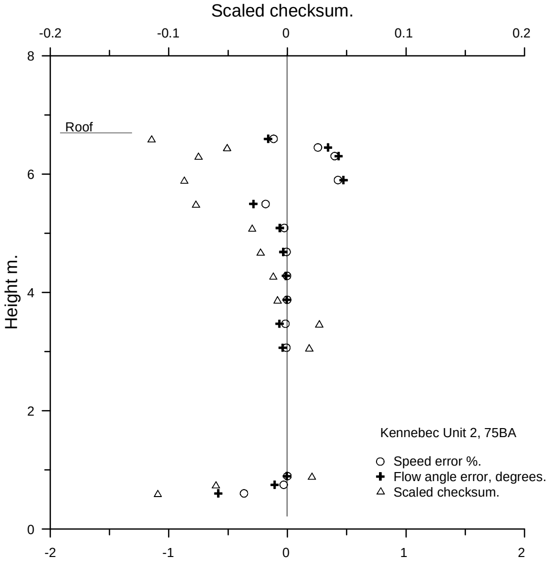

12.6. Kennebec Unit 2

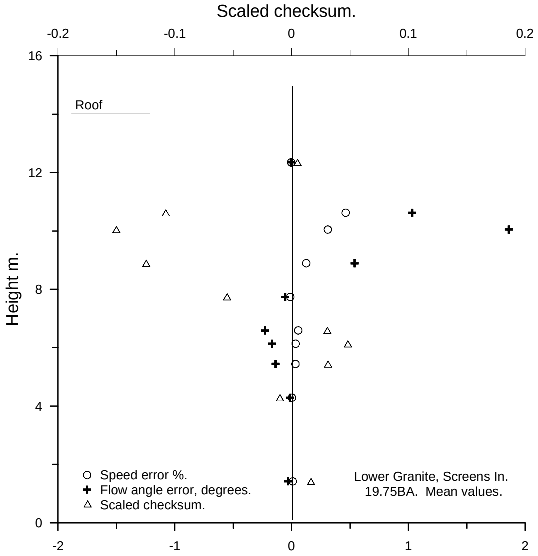

Figure 12.7. Lower Granite, screens in.

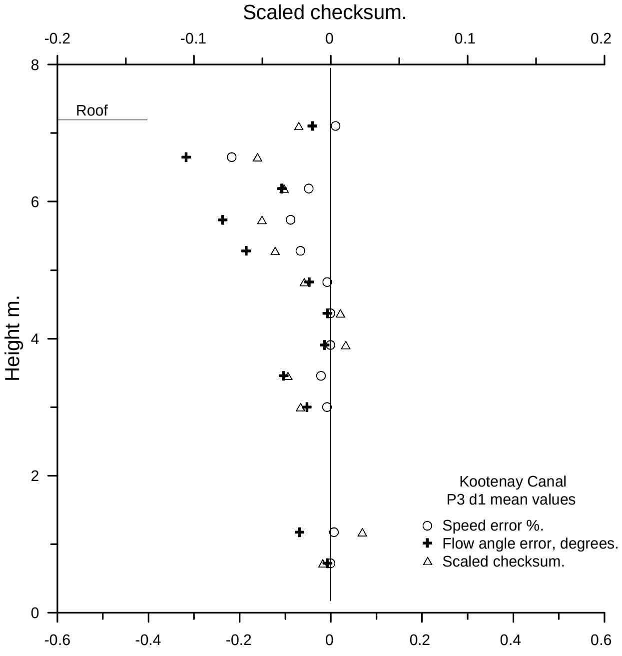

Figure 12.8 Kootenay Canal

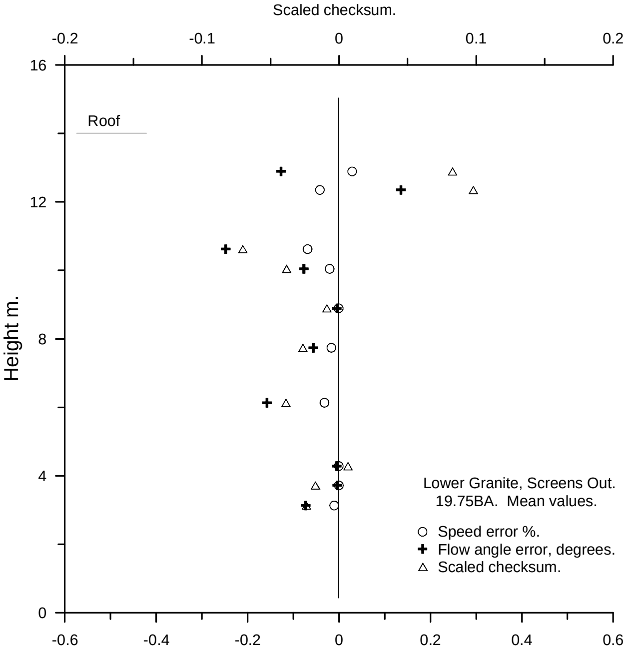

Figure 12.9. Lower Granite, screens out.

12.1 The relationship between the array orientation and the systematic errors.

The relationship between the scaled checksum, the array alignment, and the systematic errors in the output of the algorithm are explored by taking the exponential fit to a particular correlation peak locus and, taking this as an example, assuming a series of array orientation angles, and calculating the resulting values of the correlation peaks and time delays from the exponential fit. The algorithm is then applied to this simulated data and the flow speed and direction calculated from the standard algorithm, these re-calculated values now contain the errors accruing from the curvature of the correlation peak locus when viewed with a series of array orientations.

The results of applying this procedure to a particular example are shown in figure 12.10. The calculations are based on the exponential fits to data from a level just below the roof of the Kennebec plant where the correlation peak offset angle is -23^o and the scaled checksum -0.05.

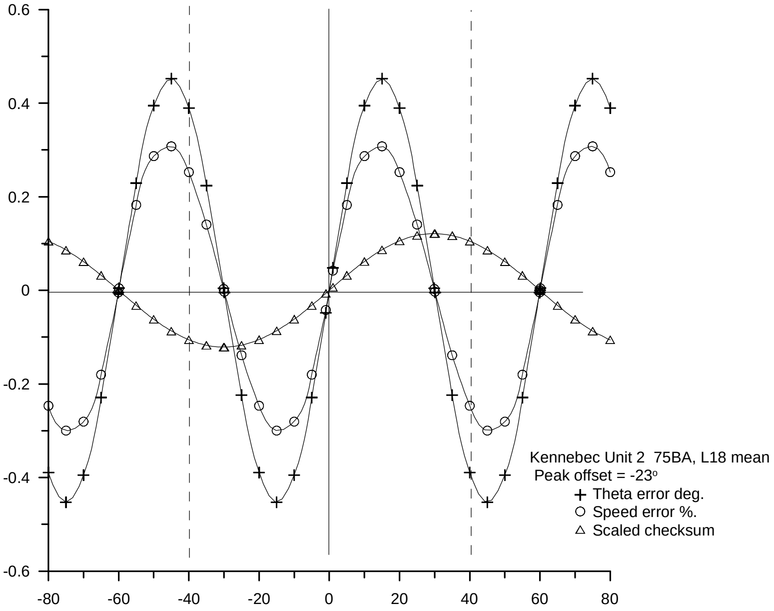

Figure 12.10 Variation of flow speed and direction error with array alignment.

Note that the systematic errors have 60^o cycles compared with the checksum cycle of 120^o. For array orientations at 0^o or 30^o to a reference correlation pair, two of the correlation peaks are of equal magnitude, and flow angle is unambiguously determined as either 0^o or 30^o, depending whether the third peak is greater or less than the coincident pair, the correlation distance being zero or a maximum. The checksum on the other hand is only zero when the array orientation is zero, attaining a maximum at 30^o intervals. When viewed in the correlation plane, the zero degree orientation places the third peak at the origin, and the radial alignment is identically satisfied; at 30^o however, the third peak lies beyond the coincident pair, maximizing the effects of the curvature. The orientation having the maximum systematic error is weakly dependent on the shape of the locus, and in this instance occurs at intervals of approximately +/- 17^{o} array alignment.

From the above analysis it can be seen that the systematic errors arising from the non-zero checksums are relatively minor and do not pose a significant problem. Their sensitivity to the array orientation allows some scope for minimization by an appropriate choice of the array mounting angle.

13.0 The relation between the anisotropy of the turbulence and the mean flow

The focus of this report has largely been on the improvements in the processing algorithm developed to account for the effects of anisotropy of the correlation field on the scintillation data. The data available to date suggests that velocity gradients in the mean flow are a major contributing factor in the generation of the observed anisotropy. In cases where significant regions of gradient in the path averaged velocities can be identified, there is a strong correlation between the velocity gradient and the correlation peak offsets. Two clear examples have been identified, the Kennebec Unit 2 and Lower Granite (Screens in) data sets, both of which exhibit regions of strong gradient in flow speed, accompanied by significant peak offset angles. Figure 13.1a shows a mean speed profile U drawn from the Kennebec data, with the corresponding gradient Grad U and correlation peak offset angle ϕ profiles shown in figure 13.1b. Note that the Grad U axis is plotted with reversed sign, and thus the strong similarity between the two profiles indicates a high degree of negative correlation.

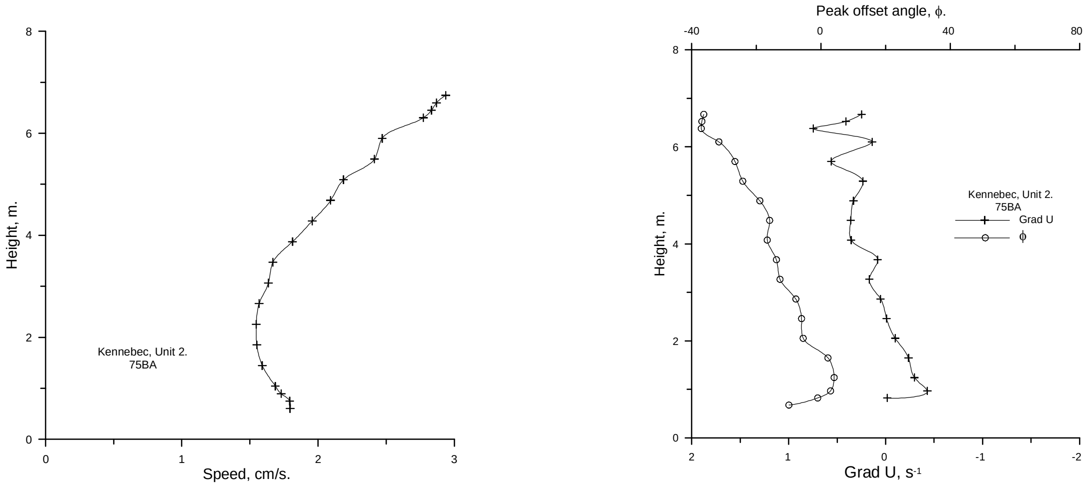

(a) (b)

Figure 13.1 Kennebec Unit 2, (a), mean speed U, (b) Grad U and ϕ.

Figures 13.2 a and b for the Lower Granite plant show superimposed speed profiles for all three bays for blade angles of 19.75 and 32 degrees respectively. The profile shapes for all three bays are closely matched, and the profiles at the two flow settings are similar in shape. The highly irregular speed profile results from the flow disturbances introduced by the fish diversion screens.

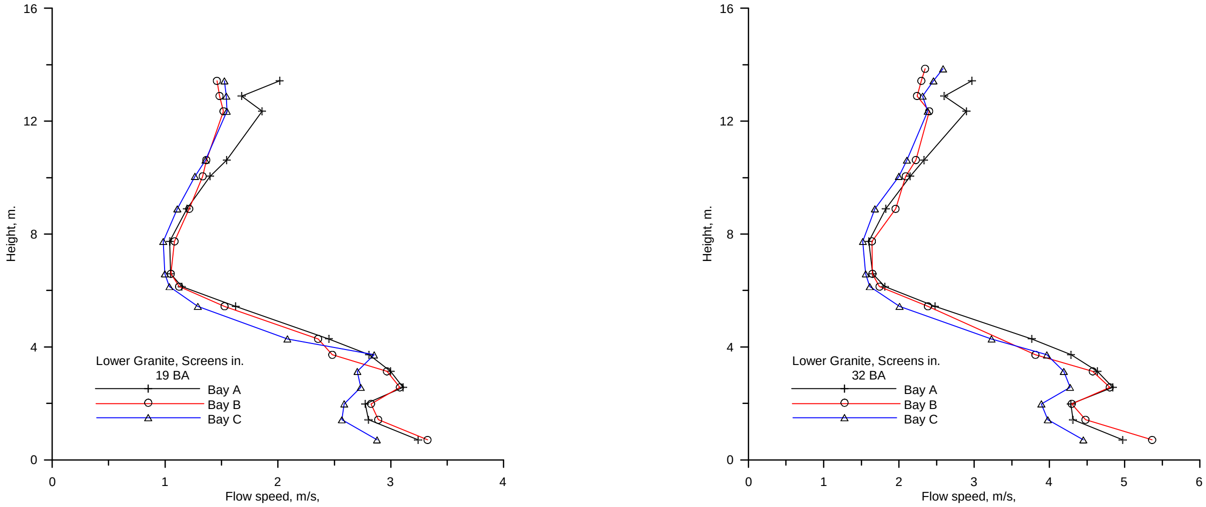

(a) (b)

Figure 13.2 Mean speed profile, Lower Granite, Screens in, (a) 19BA, (b) 32BA.

Figures 13.3a and b show the corresponding Grad *U* and *ϕ* profiles for Bay A, and as for the Kennebec data, Grad U has a high negative correlation with the peak offset angle *ϕ*. Note again that Grad U axis in the plots is reversed in sign.

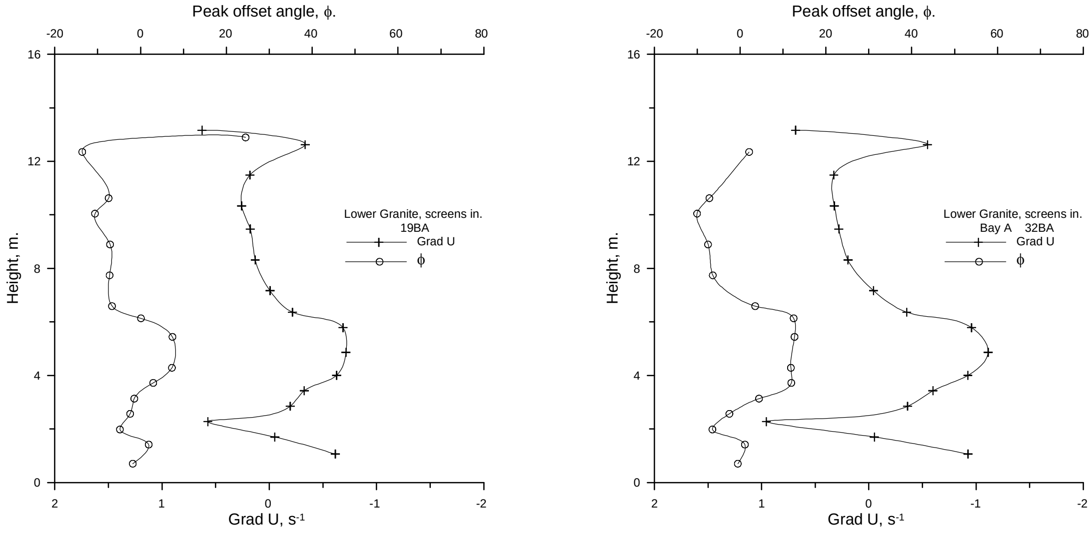

(a) (b)

Figure 13.3 Lower Granite, Bay A, Screens in, Grad U and ϕ, (a), 19.75BA, (b) 32BA.

The rotation of the cross correlation peaks in the correlation plane is generated by the response of the turbulent field to shear in the mean velocity profile. The occurrence of non-zero checksum values is also linked to the rotation of the correlation peaks via the curvature of their locus in the correlation plane. This form of anisotropy appears to be typical for the turbulence encountered in hydro-electric plant intakes where the trashrack supporting members are predominantly horizontal.

14.0 Estimating the Effects of Inhomogeneity in the Turbulence Field

The preceding analysis has concentrated on the effects of anisotropy in the turbulence on the measurement of velocity by acoustic scintillation drift under the conditions common to most hydroelectric plant intakes. Bias errors in the ASFM velocity can arise if there are coincident, strong inhomogeneities in the intensity of small-scale turbulence and the mean velocity in the measurement plane, such as are typically found in the wakes behind large supporting members in the trashracks, oriented perpendicularly to the ASFM's acoustic paths (Lemon, 2006). In the absence of such structures or other strong perturbing influences to the hydraulic conditions in the intake, the inhomogeneities in the turbulence and velocity fields are not large enough to cause measurable systematic errors in the velocity data.

The fundamental measurement that the ASFM makes is the time delay to the peak of the covariance of the log-amplitude time series from two separated acoustic paths. If the turbulence is nearly uniform along the path, then the covariance is given by equation 2.1 (repeated below as Eq. 14.1), where the turbulence level is described by the constant, C_n^2, which appears outside the integration.

$$C_\chi = 4\pi^2\alpha^2k^2C_n^2\int_0^L\int_0^\infty K^{-8/3}\sin^2\left[\frac{K^2z(L-z)}{2kL}\right]J_0\left(K\left|\vec{\rho}-\vec{V}(z)\tau\right|\right)dKdz \tag{14.1}$$

[k is the acoustic wavenumber, V(z) is the mean flow velocity as a function of position, z, along the path, ρ is the path separation, and τ is the delay.]

If, however, the level of turbulence along the path is not constant, then C_n^2 becomes a function of the path length, z and the covariance is given by equation 4-10.

$$C_\chi = 4\pi^2\alpha^2k^2\int_0^L\int_0^\infty C_n^2(z)K^{-8/3}\sin^2\left[\frac{K^2z(L-z)}{2kL}\right]J_0\left(K\left|\vec{\rho}-\vec{V}(z)\tau\right|\right)dKdz \tag{14.2}$$

The potential bias in the ASFM velocity can be estimated if information is available about the distribution of the turbulence intensity, which may be obtained either from a CFD simulation, or by using vertically-oriented paths to measure the variance of the acoustic scintillations as a function of distance across the intake (Lemon et al, 2004). The bias is then estimated by evaluating 14.2 from the distributions for the turbulence and velocity, finding the delay to its peak value, τ_0, and the resulting velocity ρ/τ_0, which may then be compared to the path average of the velocity.

15.0 Discussion and Conclusions

The acoustic scintillations sensed by the ASFM are largely generated by the trashrack structures at the entry to the intake. The characteristics of this turbulence are found to differ in important aspects from the assumptions of the original processing algorithm, introducing errors in both speed and direction. The revisions to the data processing algorithms described in this report account for these deficiencies and provide improved estimates of the flow speeds and angles.

The improvements in processing can be classed under the following headings.

> 1. Selection of the acoustic pulse rate to minimize interference from reflected pulses. The instrument is managed internally to adjust the pulse rate after monitoring an extended succession of reflected pulses. The rates are optimized independently for each level and flow condition.
>
> 2. The selection of the cut-off filter settings for the time series based on wave number rather than frequency. This ensures that the scintillations observed are derived from the same class of turbulent structure under different flow conditions.
>
> 3. The replacement of the numerical routines in the algorithm for flow speed and angle by analytical solutions. This eliminates spurious errors and allows some small systematic errors to be identified and their magnitude estimated.
>
> 3. A major feature of the trashrack generated turbulence is an anisotropy which induces additional components into the time delays, the net effect being an apparent rotation of the flow vector. This additional rotation modifies both the flow speed and direction output by the algorithm. This form of anisotropy appears to be associated with gradients in the mean flow velocity.

Modifications to the algorithm have been developed which largely correct for the anisotropy and yield substantially improved values flow angles and speed. The modified algorithm utilizes the peak correlation values, together with some assumptions as to the form of the correlation field to compute the flow angle. The speed derived from the time delays then utilizes the true value of the flow angle. Detailed examination of a number of data sets corroborates the assumptions as to the form of the correlation field.

A secondary feature the anisotropy is a slight degree of curvature in the locus of the correlation peaks. The overall effect is to introduce minor systematic errors into the flow speed and direction. The magnitude of these errors is dependent on the orientation of the transducer array to the flow direction. A procedure has been developed to estimate their magnitude. For the cases so far examined, these amount to less than 0.5% in speed and 0.5^o in angle, with the exception of areas of separated flow where reliable correlations are difficult to obtain.

The main focus of this report has been on the effects of characteristics of the turbulent flow which are common to most hydroelectric plant intakes, and are directly detectable in the data returned by the scintillation system. A separate class of error arises from non-uniform distributions of the flow properties along the length of the acoustic paths, either from vertical obstructions upstream of the measurement plane, or from uneven flows at the entry of the intake. These require additional information, either from vertical acoustic paths or CFD modeling, for the appropriate corrections to be applied. For an example demonstrating the correction procedure see Lemon et al (2004).

16.0 References

Almquist, C., J. Walsh and J. Taylor. 2011. Kootenay Canal flow rate comparison using intake methods. Hydro Vision 2011, Sacramento CA July 19-22, 2011.

Lee, Robert W. and Jeffrey C. Harp. 1969. Weak scattering in random media, with applications to remote sensing. Proc. Ieee 57, 375-406.

Lemon, D. D., 2006. Recent advances in resolving bias in discharge measurement by acoustic scintillation. Proc. IGHEM 2006, Portland, Oregon, July 2006.

Lemon, D.D., D.R. Topham, L. Bouhadji and J. Lampa, 2004. Understanding causes for systematic error in ASFM measurements of turbine discharge. Proc. Hydrovision 2004, Montreal, Quebec.

Wittinger, R.L. 2005. Absolute flow measurement in short intake large Kaplan turbines – Results of comparative flow measurements at Lower Granite powerhouse, Hydro 2005, Villach, Austria.

Wygnanski, I., F. Champagne, B. Marasli. 1986. On the large-scale structures in two-dimensional, small-deficit, turbulent wakes. J. Fluid Mech. Vol. 168, pp. 31-71.

Appendix A.
Exact solution for the flow angle from three correlation values.

It is assumed that the correlation field is self similar and that the correlation function in any given direction can be adequately represented by the scaled Gaussian distribution,

$$f_n = a\exp(-\alpha r^2)$$

The parameter α is a measure of the correlation scale length σ $(=\alpha^{-1/2})$, in general a function of the direction of the correlation.

Taking the x and y axes of the coordinate system along and normal to the flow direction, and defining the direction of the correlation by the angle ϕ, defined as positive clockwise from the y direction. Assuming that the angle ϕ is given, the correlation distance r in the direction ϕ becomes,

$$r = y_n / \cos\phi$$

The correlation coefficients for the three transducer pairs become

$$f_h = a\exp\left[\frac{-\alpha d^2 \sin^2\theta}{\cos^2\phi}\right] \qquad \text{A1}$$

$$f_v = a\exp\left[\frac{-\alpha d^2 \sin^2(60-\theta)}{\cos^2\phi}\right] \qquad \text{A2}$$

$$f_d = a\exp\left[\frac{-\alpha d^2 \sin^2(60+\theta)}{\cos^2\phi}\right] \qquad \text{A3}$$

Taking logarithms of the above equations and subtracting in pairs yields the following,

$$\ln\left(f_h / f_v\right) = C\left[\sin^2(60-\theta) - \sin^2\theta\right] \qquad \text{A4}$$

$$\ln\left(f_d / f_v\right) = C\left[\sin^2(60-\theta) - \sin^2(60+\theta)\right] \qquad \text{A5}$$

$$\ln\left(f_h / f_d\right) = C\left[\sin^2(60+\theta) - \sin^2\theta\right] \qquad \text{A6}$$

where $C = \dfrac{\alpha d^2}{\cos^2\phi}$.

Providing that the correlation field is self similar, these equations apply in a general direction ϕ. The algorithm itself is based on the correlation peak values $f_{H,}$ $f_{V,}$ f_D in the direction $\phi_{P.}$ Expressing the squared trigonometric factors in θ terms of 2θ, equations A4, A5 and A6 reduce to

$$\ln\left(f_H / f_V\right) = C\frac{\sqrt{3}}{4}\left[\sqrt{3}\cos(2\theta) - \sin(2\theta)\right] \qquad \text{A7}$$

$$\ln\left(f_D / f_V\right) = C\frac{\sqrt{3}}{2}\sin(2\theta) \qquad \text{A8}$$

$$\ln\left(f_H / f_D\right) = C\frac{\sqrt{3}}{4}\left[\sqrt{3}\cos(2\theta) + \sin(2\theta)\right] \qquad \text{A9}$$

Solving for 2θ then yields

$$\tan(2\theta) = \frac{\sqrt{3}}{(1-2\mathrm{A})} \qquad \text{A10}$$

where

$$A = \frac{\ln\left(f_H / f_V\right)}{\ln\left(f_D / f_V\right)}$$

From equation A8, we obtain,

$$C = \frac{-2\ln\left(f_D / f_V\right)}{\sqrt{3}\sin(2\theta)} \qquad \text{A11}$$

and hence

$$\frac{\cos^2\phi_P}{\alpha} = \frac{d^2\sqrt{3}\sin(2\theta)}{2\ln(f_D / f_V)} \qquad \text{A12}$$

and

$$\ln a = C\sin^2(\theta) + \ln f_H \qquad \text{A13}$$

The factor $\frac{\cos^2\phi_P}{\alpha}$ is the square of the correlation scale normal to the flow direction. Note that the flow angle θ, the factor a are independent of the correlation direction.

These equations return values of θ in the first and fourth quadrants. The basic solution is in 2θ, the parameter α changes sign at intervals of π, and quadrant decisions on θ occur at intervals of π/4, and information from the time delays is required to make the correct quadrant determination. The selection is complicated by the correlation peak offset angle ϕ which changes the phase of the time delays with respect to the true flow angle θ_f. Additional complications arise from inconsistencies in the individual time delays due to non-zero checksum values.

The conditional requirements to determine the correct quadrant are more robust if the time delays are normalized by the absolute magnitude of the largest of the three time delays.

Horizontal: $$\overset{*}{H} = \frac{DelT_H}{abs(DelT)_{Max}} \qquad \text{A14}$$

Vertical: $$\overset{*}{V} = \frac{DelT_V}{abs(DelT)_{Max}} \qquad \text{A15}$$

Diagonal: $$\overset{*}{D} = \frac{DelT_D}{abs(DelT)_{Max}} \qquad \text{A16}$$

This transforms the cosine functions of the time delays into near trapezoidal functions, as shown in the graphs below.

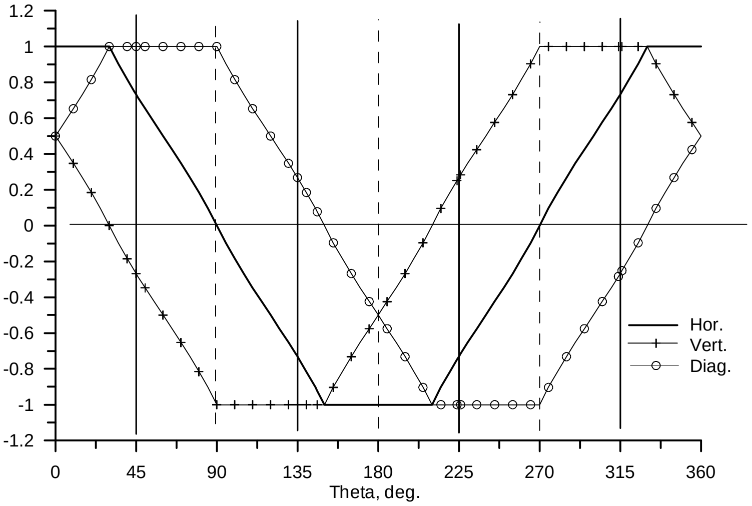

Figure A1. Normalized time delay functions, $\phi_P = 0$.

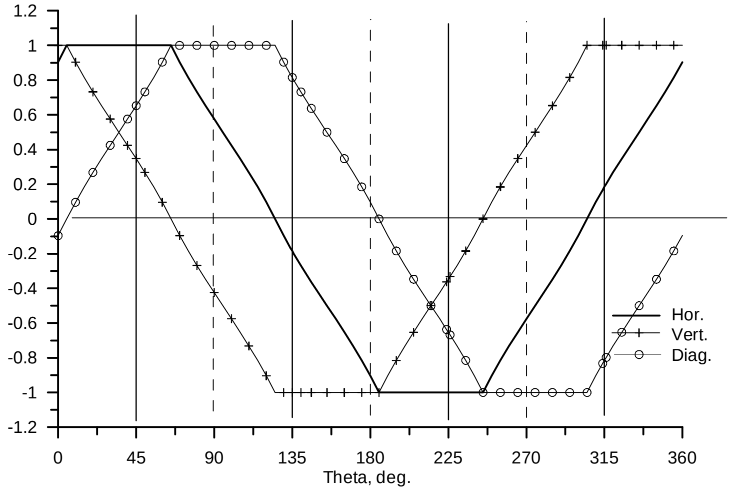

Figure A2. Normalized time delay functions, ϕ_P = -35°.

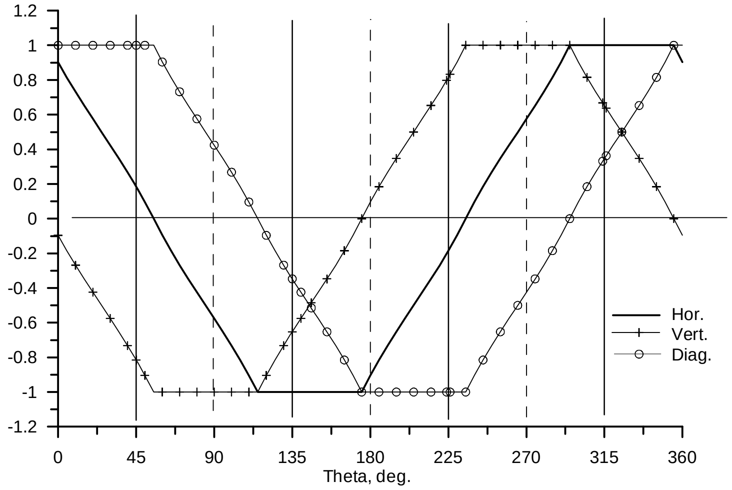

Figure 3. Normalized time delay functions, ϕ_P = +35°.

The following table details the conditions to be satisfied for the correct quadrant selection.

θ_f	-45 to +45	+45 to 135		135 to 225	225 to 315	
		45 to 90	90 to 135		225 to 270	270 315
	α +ve	α -ve	α -ve	α +ve	α -ve	α -ve
	$H^*>0$	$V^*>0$	$D^*<0$	$H^*<0$	$V^*<0$	$D^*>0$
		$V^*>D^*$	$V^*>D^*$		$D^*>V^*$	$D^*>V^*$
$\Delta\theta$	0	90		180	270	

For a fully internally consistent set of time delays these conditions return an unambiguous quadrant selection over the range of peak offset angle of ϕ_P -44° to +44°. Outside this range, two quadrant conditions separated by 180° are satisfied simultaneously, but in this case the angle returned by the least squares numerical routine is closest to the correct quadrant choice. A similar problem occurs with non-zero time delay checksums, but in this case a single quadrant choice in error by 180° is offered, but here again a comparison with the least squares numerical routine identifies the necessary correction.

Once the correct quadrant is identified, the solution angle θ can be corrected by the addition of the quadrant correction angle

$$\theta_f = \theta + \Delta\theta$$

and the values of α and '*a*` recalculated.

Additional constraints

The base line solution itself has problems under the following conditions:

1. $A \to \infty$.

This occurs for $\theta_f = 0$ and 180° when $\ln(f_D / f_V) = 0$ and the equation

$$\alpha = -\frac{2}{d^2\sqrt{3}}\frac{\ln(f_D / f_V)}{\sin 2\theta}$$

is indeterminate.

If however we write

$$\ln(f_D / f_V) = \frac{\ln(f_H / f_V)}{A}$$

Since 2θ is small, sin(2θ) can be replaced by tan(2θ), , the equation becomes,

$$\alpha = \frac{-2\ln(f_H / f_V)}{3d^2}\frac{(1-2A)}{A}$$

For large A, which is the case under consideration,

$$\alpha = \frac{4}{3d^2}\ln(f_H / f_V) \qquad \text{A16}$$

2. A = 0.5

If A = 0.5 exactly, a division by zero error occurs as $\tan(2\theta) \to \pm\infty$.

This arises at $\theta = 45^\circ$, $\theta = 135^\circ$, $\theta = 225^\circ$, $\theta = 315^\circ$.

If A approaches 0.5 from below, ie A = 0.5 - δ

$$\tan(2\theta) \to +\infty \text{ and } \sin(2\theta) \to +1$$

$$\alpha = -\frac{2}{d^2\sqrt{3}}\ln(f_D / f_V) \qquad \text{A17}$$

Likewise, if A approaches 0.5 from above, ie A = 0.5 + δ

$$\tan(2\theta) \to -\infty \text{ and } \sin(2\theta) \to -1$$

and $$\alpha = +\frac{2}{d^2\sqrt{3}}\ln(f_D / f_V) \qquad \text{A18}$$

The value of the small parameter δ required to limit the employment of the original equation is determined by the particular software employed.

Appendix B.

An elliptic representation of the anisotropy.

The measured correlation fields in many cases approximate to elliptic anisotropy distributions, as in the example shown in figure 8.1, a form which lends itself to analytical treatment.

The correlation function is assumed to have the Gaussian form

$$f(y,\phi) = a\exp\left(-\frac{y^2}{\cos^2(\phi)\sigma_o^2 k^2}\right) \qquad \text{(B1)}$$

where y is the distance normal to the flow direction, and ϕ the direction of the correlation, measured clockwise from the normal.

The standard equation for the ellipse with major and minor axes a and b expressed in the polar coordinates k, γ is,

$$\frac{1}{k^2} = \frac{\cos^2\gamma}{a^2} + \frac{\sin^2\gamma}{b^2}\ , \qquad \text{(B2)}$$

where k represents the scale factor of the assumed Gaussian form of the correlation distribution defined by (B1).

The field data shows that in general the anisotropy distribution is inclined at an angle to the flow direction, and an appropriate representation of the distribution is then an ellipse of major and minor axes of a = 1 and b = β respectively, inclined at an angle ω to the flow direction.

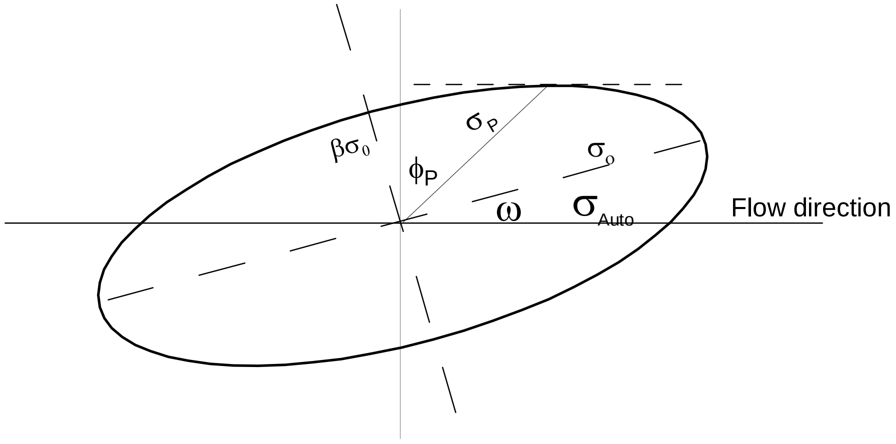

Figure B1. Geometry of the anisotropy ellipse.

The polar angle of the ellipse, $\gamma = 90 - (\varpi + \phi)$, and the function *k(ϕ)* is thus,

$$k^2 = \frac{\beta^2}{\cos^2(\omega+\phi) + \beta^2 \sin^2(\omega+\phi)} \qquad \text{(B3)}$$

The exponent in the equation (B1) is then

$$-\frac{y^2\left[\cos^2(\omega+\phi) + \beta^2 \sin^2(\omega+\phi)\right]}{\sigma_o^2 \beta^2 \cos^2\phi}$$

where ω is the angle the major axis of the ellipse makes with the flow direction, measured positive anticlockwise.

The peak of the correlation curve corresponds to the condition that

$$\cos^2(\phi)k^2$$

is a maximum, ie the point on the ellipse where the tangent is parallel to the flow direction, or from equation B3, when

$$\frac{\cos^2\phi}{\left[\cos^2(\omega+\phi) + \beta^2 \sin^2(\omega+\phi)\right]} \quad \text{is a maximum.} \qquad \text{(B4)}$$

.

This occurs when (noting that the sign convention chosen for ϕ is positive clockwise, opposite to that of ω)

$$\tan\phi_{Peak} = \frac{\left(1-\beta^2\right)\tan\varpi}{\beta^2 + \tan^2\varpi} \qquad \text{(B5)}$$

The peak offset in the flow direction is $y\tan\phi$, hence

$$x'_{Offset} = y\frac{\left(1-\beta^2\right)\tan\varpi}{\beta^2 \tan^2\varpi} \qquad \text{(B6)}$$

Application of the result (B5) then gives the value of k^2 corresponding to the peak correlation value. The maximum displacement of the peaks occurs at

$$\cos(2\omega) = \frac{(1-\beta^2)}{(1+\beta^2)}$$

Where +/- ω defines the maxima of the positive and negative displacements of the peaks respectively. Figure B2 shows the variation of the angle ϕ_{Peak} with both β and ω.

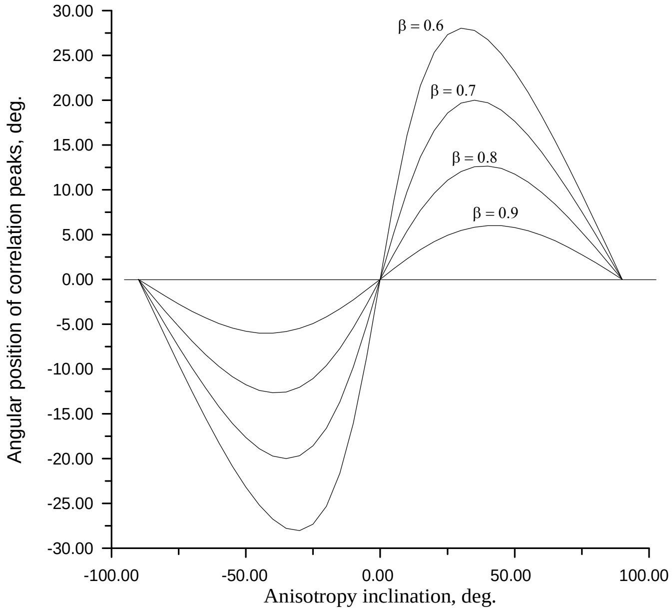

Figure B2

The values of the correlation scale factor corresponding to the correlation peaks, σ_p and the auto correlation function $\sigma_{Auto,}$ together with the peak offset angle ϕ, can be calculated from the flow solution, and are sufficient to derive the parameters of the correlation ellipse.

$$\sigma_p^2 = \frac{\sigma_o^2 \beta^2}{\cos^2(\omega+\phi_p) + \beta^2 \sin^2(\omega+\phi_p)}$$

(B7)

$$\sigma_{Auto}^2 = \frac{\sigma_o^2 \beta^2}{\cos^2\omega + \beta^2 \sin^2\omega} \quad \text{since } \phi = 90^{\circ} \qquad \text{(B8)}$$

The following relationships can then be derived

$$\tan\varpi(1-\tan\phi_p \tan\omega)(\tan^2\varpi - D) = (D\tan^2\varpi - 1)(\tan\phi_p + \tan\varpi) \qquad \text{(B9)}$$

$$\beta^2 = \frac{D\tan^2\omega - 1}{\tan^2\varpi - D} \qquad \text{(B10)}$$

where $D = \dfrac{1 + C\sin^2\phi_p}{C\cos^2\phi_p}$, and $C = \dfrac{\sigma_p^2}{\sigma_{Auto}^2}$

Equation B9 is solved numerically for ω and hence β can be obtained.

The scale factor σ_o can then be obtained from B.8.

Appendix C.
Revised Filtering Procedure for ASFM data.

The raw acoustic amplitude time series used in the acoustic scintillation method are band-pass filtered before computing the cross-correlations used to calculate the velocity. The original filtering procedure used at both Lower Granite and Chief Joseph Dam used a fixed value of 40 Hz for the upper limit to the passband, while the lower limit was selected using an iterative procedure. The lower cut-off was varied between 0.5 Hz and 15.5 Hz in steps of 1 Hz. The velocity was computed for each selection, and the selection which gave the highest quality index was used for the reported velocity. The time series was divided into 2048-point blocks, with a velocity computed for each block. Outliers from that set of velocities were rejected using the Grubbs T-statistic, and the velocity used in the discharge was then the average of the individual velocities of the remaining blocks. The quality index is the product of the mean peak cross-correlation score multiplied by the fraction of the blocks that were retained.

The revised procedure addresses limitations arising from the fixed range over which the lower passband limit was chosen, and also modifies the way the correlation results are used to compute the velocity. The turbulence that produces the acoustic scintillations occupies a fixed range of spatial scales; the range of frequencies they produce in the acoustic time series therefore varies with the mean flow speed. The previous procedure did not account for this effect, and therefore was not always properly aligned with the wavenumbers producing the scintillations. The passband selection procedure has been modified to address that limitation. The passband frequency limits are selected from one of five sets, designed to maintain the same wavenumber range in the turbulence as the source of the amplitude fluctuations. An initial estimate of the flow velocity computed from data filtered with a fixed passband of 6.5 to 40 Hz is used to select the passband limit set; the upper limit of each set is fixed, and the lower limit is selected from a range of frequencies specific to each set. The selection is an interative process; the lower limit frequency, f_L, is incremented in steps from the minimum to the maximum of the range for the first few blocks of data. The ranges and step sizes are shown in the table below:

Initial Velocity Estimate (m/s)	Upper Band Limit (Hz)	Range for Selection of Lower Band Limit (Hz)	Frequency Step Size (Hz)
$V < 1.5$	40	1 - 7	0.5
$1.5 \le V < 2.5$	45	2 - 14	1
$2.5 \le V < 3.5$	50	3 - 21	1.5
$3.5 \le V < 4.5$	55	4 - 28	2
$4.5 \le V < 6.0$	60	5 - 35	2.5

The peak cross correlation values for the three pairs of time series for each block are recorded, and those above a threshold value of 0.2 (the theoretical minimum) are retained. A quality index, QI, is then computed as the product of the ratio of the average peak correlation score for each pair to the theoretical maximum and the fraction of the scores that were retained as being above the threshold value. The procedure is repeated for each value of f_L, and the value with the highest QI is used to filter the entire data set. The three peak cross-correlations and time delays for each block are then computed. The velocity is computed from their averages, after rejection of outliers, which are rejected using the Grubbs T-statistic. For example, in a 6 block set, values more than 1.89 standard deviations from the mean are removed. The quality index QI is recomputed after outlier rejection. Using the averages of the correlation peak scores and time delays to compute the velocity retains more of the data than the original procedure, since blocks that were rejected for invalid velocities previously may still contain one or more valid correlation values. The revised procedure allows those values to be used.